UNIVERSITY OF AMSTERDAM

MSc Physics

Science for Energy and Sustainability

Master Thesis

Wide-Angle, Broadband Graded Metasurface for Back Reflection

---

by

Verena Neder

Stud.nr: 10850481

June 2016

60 ECTS

September 2015 - June 2016

1st Examiner:

Prof. Albert Polman

2nd Examiner:

Prof. Tom Gregorkiewicz

Supervisor:

Dr. Mark Knight

Abstract

Gradient metasurfaces enable a large degree of control over reflection and transmission of light, while using low-profile and low-loss patterned surfaces. Here, we demonstrate near-unity back reflection with a gradient metasurface tailored for wavelength of 700 nm and incoming angle of 35.7 degrees. The experimental work is based on the Huygens-Fresnel principle for tailoring light scattering at will through engineered phase fronts. The optimized geometry is capable of efficiently redirecting s-polarized light into the first negative diffraction order over a broad range of angles and frequencies. The theoretical geometry was experimentally realized over a 2x2 mm^2 area, with angle-resolved optical measurements confirming the high predicted efficiencies. The metasurface consists of a non-symmetric, subwavelength, 1D grating comprised of two high-index (n=2.26) TiO_x bars in each unit cell (periodicity of 605 nm), placed on a protected Ag mirror, and was fabricated by electron beam lithography. Quantitative optical measurements show that an absolute coupling efficiency of s-polarized light to the first negative diffraction order above 85% is achieved at 700 nm for $\pm(20 - 60)$ degrees. For the Littrow configuration, (700 nm, 35.7 degrees) we measure 88% efficiency. The efficiency is primarily determined by the quality of the evaporated mirror, with the unpatterned Ag layer producing nearly identical absorption losses. A remarkable property of this device resides in the broad operational bandwidth, which can be explained by the non-resonant nature of the TiO_x scattering elements comprising the metasurface. Simulations show that the metasurface functions over an extremely broad wavelength range (490 – 940 nm) with a coupling efficiency above 50% for angles between $\pm(24 - 51)$ degrees, and have been confirmed by optical measurements at 750 nm and 850 nm. Another interesting feature is the angularly symmetric optical response of the asymmetric surface, which stems from reciprocity considerations. More broadly, our work shows that designer metasurfaces operating over broad frequency and angular bandwidths and with high efficiency, become competitive alternatives to traditional volumetric optical components for a wide range of light management applications.

Contents

1 Introduction **1**

2 Theory: Phase profile for back reflection **3**

2.1 Generalized law of reflection: Derivation of phase profile from ray-optics approach . . . 3

2.2 Huygens' surfaces: Derivation of reflection coefficient from full wave approach 5

2.3 Calculation of coupling efficiency of ideal phase profile . . . 6

2.4 Development of graded metasurface design . . . 8

3 Experimental realization of graded metasurface **10**

3.1 Assymetric grating with graded effective index . . . 10

3.2 Bottom up technique . . . 11

3.2.1 Bottom up fabrication of graded metasurface . . . 11

3.2.2 Challenges of bottom up fabrication . . . 13

3.3 Top down technique . . . 14

3.3.1 Top down fabrication of graded metasurface . . . 14

3.3.2 Challenges of TiO_x RIE etching . . . 16

4 FEM and FDTD modeling of metasurface back reflector **18**

4.1 Simulation methods . . . 18

4.1.1 Frequency-domain modeling by FEM . . . 18

4.1.2 Time-domain modeling by FDTD . . . 19

4.2 Modeling of optical response of graded metasurface . . . 20

4.2.1 Coupling efficiencies at different wavelengths . . . 20

4.2.2 Coupling efficiency for N=2 and N=3 discretization . . . 21

4.2.3 Angular/wavelength dispersion . . . 22

5 Optical measurements on metasurface back reflector **23**

5.1 Optical visualization of back reflection . . . 23

5.2 Optical measurement setup: Rotating stage . . . 23

5.3 Optical response of graded metasurface . . . 26

5.3.1 Coupling efficiency at ideal wavelength . . . 26

5.3.2 Coupling efficiency at different wavelengths . . . 29

5.3.3 Polarization dependence of the back reflector . . . 29

5.3.4 Laser diode measurement for result confirmation . . . 31

5.3.5 Coupling efficiency for N=2 and N=3 discretization . . . 32

6 Discussion, conclusion and outlook **34**

A Appendix **36**

A.1 Determination of dielectric constants of TiO_x using ellipsometry 36

A.2 Determination of period of fabricated structure 36

A.3 Original data of optical measurement of structure with N=2 and N=3 . . 37

1 Introduction

Gradient metasurfaces have started to significantly affect modern optical technology as they offer the possibility of replacing a wide range of bulky optical components with low-profile and low-loss patterned surfaces [1–4]. Graded metasurfaces rely on nanostructured surfaces with controlled variation of their transverse impedance, enabling a large plethora of operations, including anomalous wave refraction and reflection [5], holography [6, 7], cloaking [8–10], focusing and beam shaping [5, 11], polarization management [8, 12], and nonreciprocal beam control when combined with time modulation [13, 14]. The locally controlled nature of strong wave-matter interactions at the nanoscale in metasurfaces has opened remarkable opportunities for low-loss, integrable planarized optics [2].

In contrast to other ultrathin configurations based on resonantly excited elements [15–19], gradient metasurfaces rely on the response of a combination of non-resonant scatterers and their tailored arrangement, thus providing inherently broadband, robust response resilient to losses [8]. In this work, the concept of graded metasurfaces to design broadband back reflectors is applied, based on distributed surface impedances.

Back reflectors are traditionally implemented with binary patterns [17, 20–22] that can be optimized [22, 23] to maximize the coupling efficiency to the backward Floquet order s_1^-. In contrast, here the Huygens–Fresnel principle is used to define the ideal surface impedance profile of ultrathin metasurfaces for arbitrary retro-reflection. The ideal operation of the designed surface is achieved by controlling the number, geometry, and position of high-index, dielectric nanoscale scatterers within a single wavelength to reconstruct the desired Floquet order, offering large flexibility, large efficiency over the desired range of angle of incidence (AOI), angle of reflection and frequency, without the need of optimization or specific material parameters. These concepts are experimentally verified by building a graded metasurface that operates in the visible range, employing high-resolution nanolithography.

First the study is focused on the design of an ideal gradient metasurface that reflects back all the impinging energy for a specific frequency and angle for linear polarized light. This functionality is equivalent to an 1-dimensional ideal retroreflector for this frequency and AOI, and provides negative reflection in the general case (Fig. 1 (a) shows the concept and a schematic of the fabricated structure). While an ideal homogeneous mirror (Fig. 1 (b)) reflects the impinging light towards the specular direction (s_0^-) due to momentum conservation, an ideal metasurface with a tailored gradient of the reflection phase (Fig. 1 (c)) can impart a suitable additional negative transverse momentum to the impinging wave, reflecting the entire impinging light flux back to the source (s_1^-).

The functionality of the realized structure in this work is restricted to 1 dimension and

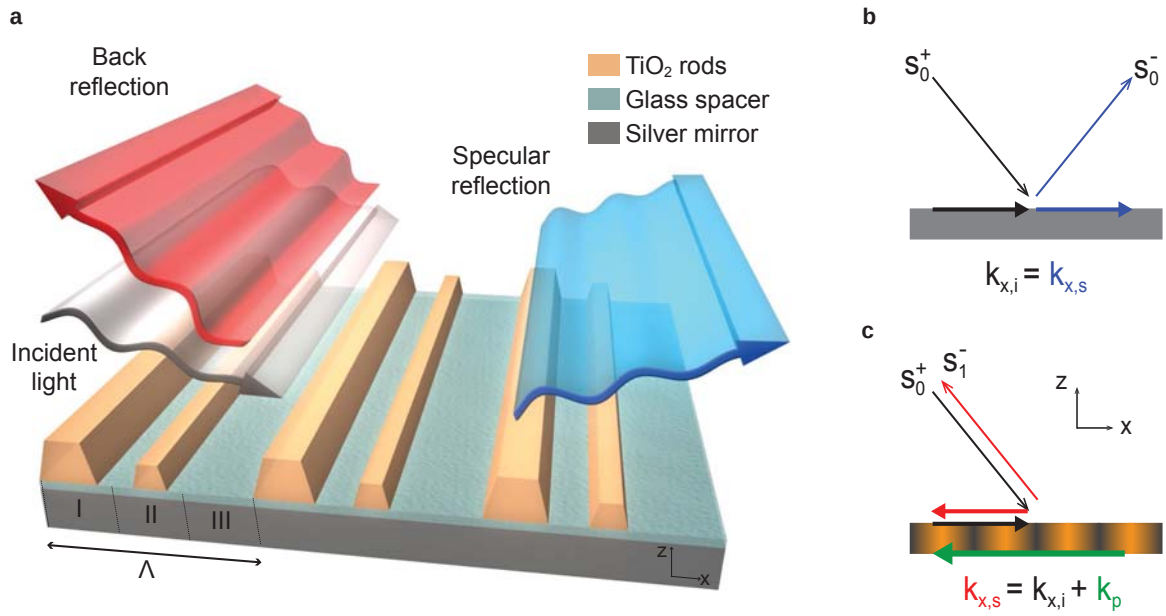

Figure 1: Operation principle of a metasurface back reflector . (a) Schematic illustration of back-reflection from a gradient metasurface. (b,c) Illustrative representation of scattering channels. (b) Specular reflection from an ideal mirror: incident light (s_0^+,black) is specularly reflected (s_0^-,blue) from an ideal mirror due to momentum conservation at the interface. (c) Retroreflection from a gradient metasurface: incident light is reflected back (s_1^-,red) toward the source due to the transverse momentum imparted by the inhomogeneous interface. The additional negative momentum k_p (green) is introduced by a tailored gradient of the reflection phase. Momenta in the x-direction are shown by $k_{x,i}$ and $k_{x,s}$ for incident and reflected waves, respectively.

therefore corresponds to a grating optimized for the Littrow configuration. The geometry of a grating that leads to diffraction of planar wavefronts is depicted in Fig. 2. A plane wavefront, incident at θ_{in} on a grating with a regular period Λ is diffracted from the grooves at an angle θ_{out}. The path difference diffracted by successive grooves is $\Lambda sin(\theta_{in}) - \Lambda sin(\theta_{out})$. If this path difference is an integer multiple of the wavelength λ, the diffracted light is in phase and constructive interference appears while the light interferes destructively otherwise. So the light is diffracted into a specific direction, given by the grating equation [24]:

$$\sin(\theta_{out}) = \sin(\theta_{in}) + \frac{m\lambda}{\Lambda} \tag{1}$$

Here, λ is the wavelength of the light and the integer $m = 0, \pm1, \pm2, ...$ describes the orders of diffraction, with the specular reflection numbered by m=0. The special case where the light is directed back exactly to the same angle $\theta_{out} = -\theta_{in}$ is called the Littrow configuration and the grating equation simplifies to:

$$\frac{m\lambda}{\Lambda} = -2\sin(\theta_{in}) \tag{2}$$

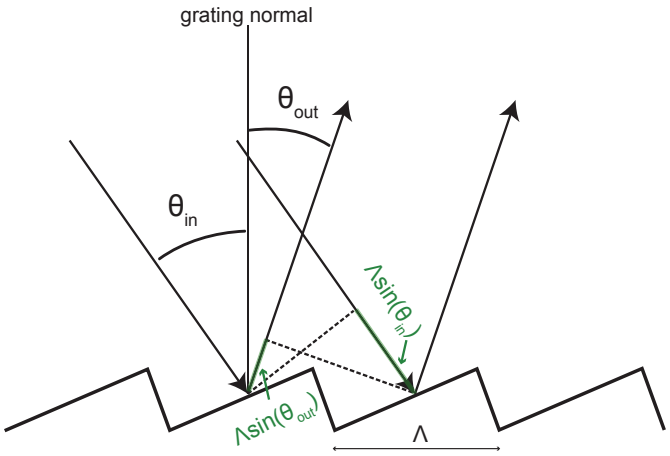

Figure 2: Geometry of diffraction grating. A planar wavefront is incident with θ_{in} on a grating with period Λ. Light that is in phase after diffraction interferes constructively at an angle θ_{out} following the diffraction equation. Figure based on [24].

.

2 Theory: Phase profile for back reflection

As motivated in the introduction arbitrary retro-reflection can be achieved by tailoring the gradient of the reflection phase of a surface. This chapter gives an introduction based on ray optics, and then provides a full wave derivation for the reflection phase gradient. Following the approach introduced in [5, 11], and tailored to efficiently manipulate reflected beams in [8], the local complex reflection coefficient that an ultrathin metasurface needs to support to achieve retroreflection with unity efficiency for a specific wavelength and angle is derived.

First a summary of the ray optics approach for light propagation with phase discontinuities is given which leads to the generalized law of reflection [5]. From there the desired phase gradient can be determined. Next, a full wave derivation is performed to design in a more accurate way the varying phase response of a reflective Huygens' surface, based on controlled variation of its transverse impedance [8, 11].

2.1 Generalized law of reflection: Derivation of phase profile from ray-optics approach

Fermat's principle states that the light always takes the trajectory that has the least optical path. More general, Fermat's principle is the principle of stationary phase. The total phase accumulated along the light path from point A to point B $\int_A^B d\phi(\vec{r})$ is constant with respect to infinitesimal changes of the path:

$$\delta \int_A^B d\phi(\vec{r}) = 0 \tag{3}$$

Light with the wavevector $\vec{k}$ that propagates along a path AB has a phase change of $\int_A^B \vec{k} \cdot d\vec{r}$. If an additional phase shift $\Phi(\vec{r_s})$ is introduced in the optical path along the interface of two media, where $\vec{r_s}$ describes the position on the interface, the total phase shift is $\Phi(\vec{r_s}) + \int_A^B \vec{k} \cdot d\vec{r}$ and is stationary following the principle of stationary phase. A generalized law of reflection is then required that takes this abrupt phase shift into account.

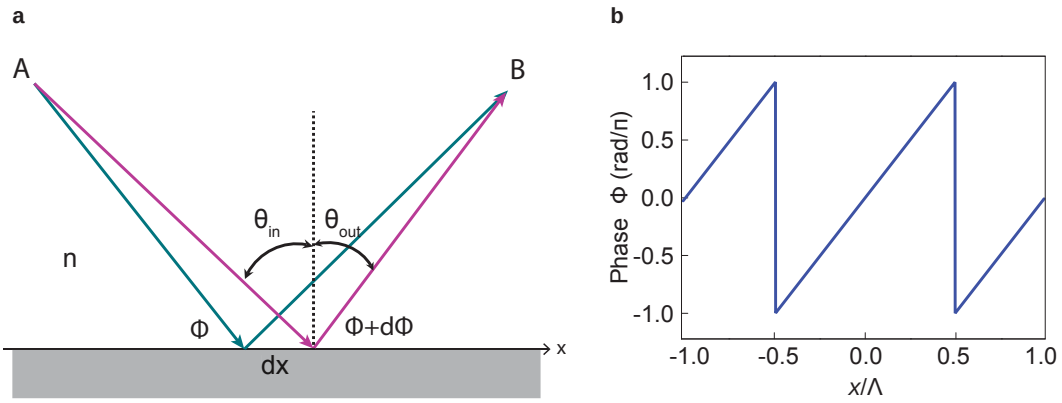

Figure 3: Schematic to derive generalized law of reflection and phase profile of constant phase shift. (a) An additional phase shift, depending on the position along the interface, is imprinted on the light by a designed metasurface. The green light path gets an additional phase shift Φ and the pink one an additional phase shift $\Phi+d\Phi$ when they are reflected on the interface. (b) General phase profile for back reflection of light with the wavelength λ to the incoming angle θ_{in} derived from the generalized law of reflection. The period of the sawtooth phase is $\Lambda = \frac{\lambda}{2\sin(\theta_{in})}$.

The phase shift of two reflected plane waves, incident on an interface at an angle θ_{in} and reflected at an angle of θ_{out} is considered (See Fig. 3). At the surface an additional phase shift Φ and $\Phi + d\Phi$ is imprinted on the waves, respectively. As the two light paths are infinitesimally close to the actual light path, the phase difference between them is zero:

$$[k_0 n \sin(\theta_{in})dx + (\Phi + d\Phi)] - [(k_0 n \sin(\theta_{out})dx + \Phi] = 0 \tag{4}$$

where Φ and $\Phi + d\Phi$ are the additional phase jumps at the locations where the two paths are reflected at the interface. n is the refractive index of the propagation medium and $k_0 = \frac{2\pi}{\lambda_0}$ the free space wave number with the free space wavelength λ_0. A constant phase gradient $d\Phi/dx$ along the interface leads to the generalized law of reflection:

$$\sin(\theta_{in}) - \sin(\theta_{out}) = \frac{\lambda}{2\pi n}\frac{d\Phi}{dx} \tag{5}$$

If there is no phase gradient along the surface ($d\Phi/dx = 0$), as is the case for normal planar interfaces, Eq. 5 simplifies to Snell's law of reflection $\theta_{in} = \theta_{out}$. Here, the concept

of a phase gradient on an interface was used to design an ideal retroreflector for one specific wavelength and AOI. The law of reflection that should be achieved is therefore $\theta_{in} = -\theta_{out}$ which, in air, leads to a needed constant phase gradient of $\frac{d\Phi}{dx} = \frac{4\pi \sin(\theta_{in})}{\lambda}$. As the phase can only reach values between 0 and 2π the required phase gradient for back reflection of light with the wavelength λ is periodic:

$$\frac{d\Phi}{dx} = \frac{2\pi}{\Lambda} \text{ with the period } \Lambda = \frac{\lambda}{2\sin(\theta_{in})} \tag{6}$$

For retroreflection the condition for the period of the phase gradient accords to the grating equation in Littrow configuration in Eq. (2). This phase profile, as function of x/Λ has then the shape of a sawtooth and is depicted in Fig. 3 (b). This ansatz is based on a ray optics approach. More accurate results require a full wave derivation.

2.2 Huygens' surfaces: Derivation of reflection coefficient from full wave approach

Following Huygens–Fresnel principle to achieve the arbitrary scattering field distribution, the electromagnetic boundary conditions of the system in Fig. 1 for s-polarized illumination read [11, 12]:

$$2\hat{z} \times (\mathbf{H}_i + \mathbf{H}_s)|_\lambda = Y_e(x)\hat{y} \cdot (\mathbf{E}_i + \mathbf{E}_s)|_\lambda \tag{7}$$

for any position x on the inhomogeneous metasurface λ, where Y_e and Z_m are the effective surface electric admittance and surface magnetic impedance of the structure. Subscripts i and s indicate the incident and reflected waves, respectively. The local reflection coefficient of the metasurface $r(x) = A(x)e^{j\Phi(x)}$ can be related to the effective properties of the surface for normal illumination as [11, 25]:

$$r(x) = -\frac{2(\eta_0^2 Y_e(x) - Z_m(x))}{(2 + \eta_0 Y_e(x))(2\eta_0 + Z_m(x))} \tag{8}$$

Considering plane wave excitation at θ_0 in the $x-z$ plane and ideal operation - *i.e.* unity retroreflection - the incident and scattered waves read:

$$\mathbf{E}_{i,s} = E_0 \exp(i(\hat{x} \cdot \mathbf{k}_{i,s}x + \hat{z} \cdot \mathbf{k}_{i,s}z)) \text{ and } \eta_0 \mathbf{H}_{i,s} = \mathbf{k}_{i,s} \times \mathbf{E}_{i,s} \tag{9}$$

where $\mathbf{k}_i = k_0(-\sin(\theta_0)\hat{x} + \cos(\theta_0)\hat{z})$, $\mathbf{k}_s = -\mathbf{k}_i$, and k_0 is the free-space wave number. Combining 7, 8, and 9 the local reflection coefficient is found. The analytical expression of the local reflection coefficient that an ultrathin metasurface needs to support to achieve retroreflection with unity efficiency for illumination angle θ_0 in the $x-z$ plane is derived, where $\hat{z}$ is the normal to the surface:

$$r(x) = \frac{-1 + \cos\theta_0 - e^{\frac{2i\pi x}{\Lambda}}(1 + \cos\theta_0)}{-1 - \cos\theta_0 + e^{\frac{2i\pi x}{\Lambda}}(-1 + \cos\theta_0)} \tag{10}$$

Note that the local complex reflection coefficient is merely a phase distribution imprinted on the reflected wave as $A(x) = 1$. The phase profile for an ideal retroreflector with θ_0=35.7 degrees is shown in Fig. 4 (a).

The required reflection coefficient is unitary across the surface, implying that it can be achieved with a fully passive interface with inhomogeneous phase profile $\Phi(x)$, shown in Fig. 4 (a) for θ_0=35.7 degrees, with period $\Lambda = \frac{\lambda}{2sin\theta_0}$, where λ is the wavelength of operation in free-space. This phase profile compensates for the momentum mismatch between the incoming and the desired retroreflected waves (Fig. 1 c). Again, the periodicity condition is equivalent to the Littrow configuration. The obtained phase profile by the full wave derivation is similar to the one derived in the ray optics approach. The important advantage of our approach compared to previous attempts to realize highly efficient gratings is to derive the electromagnetic properties of the metasurface based on the Huygens–Fresnel principle, which allows us to essentially engineer the scattering pattern of the surface at will [26]. For instance, the grating can be equivalently designed to couple half of the power towards specular reflection, and the other half towards back reflection. This freedom in the design is beyond the scope of techniques relying on optimization or excitation of certain resonant modes in the structure to support negative reflection. Due to the low dimensionality of the 1-dimensional design the resulting optimized geometry corresponds to a Littrow grating. The concept of a grating and more specific of a grating in Littrow configuration is explained in the introduction of this work. However, as the theoretical concept is fully applicable to both 2-dimensional designs and arbitrary scattering patterns the specific functionality as a Littrow grating is not discussed further.

2.3 Calculation of coupling efficiency of ideal phase profile

For an ideal continuously modulated metasurface with local reflection of Eq. (10), given the periodicity of the reflection phase, the reflected power can couple to only two propagating diffraction orders, the specular reflection $s_0^-$and the first negative diffraction order s_1^-. The numerically calculated coupling efficiency to these orders as a function of illumination angle is shown in Fig. 4 (b) for the surface with phase profile in Fig. 4 (a). The variation in the phase of the local reflection coefficient is effectively implemented by varying the surface admittance at a subwavelength distance from an ideal mirror (a perfect electric conductor) following the method described in [8]. The obtained surface profile is modeled as a sheet admittance in COMSOL as described in detail in chapter 4.1.1.

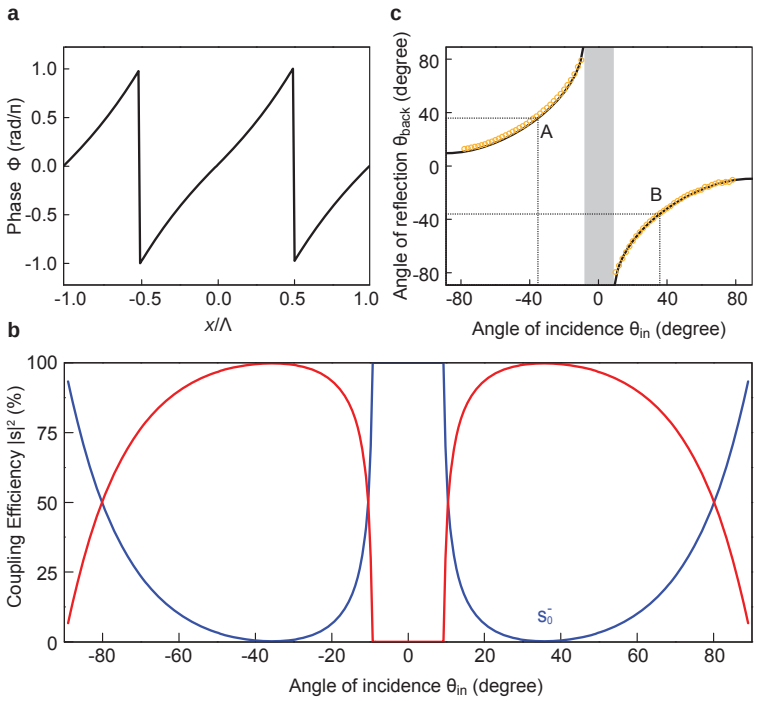

Figure 4: Wide angle operation of an ideal retroreflective metasurface (a) Calculated local phase profile of the ideal surface $\Phi(x) = \angle r(x)$, designed for retroreflection at AOI $\theta_{in} = 35.7$ degrees following Eq. (10), with surface period $\Lambda = \lambda/(2\sin(\theta_0))$. (b) Numerically calculated coupling efficiency of the ideal surface in panel (a) for different incident angles and for s-polarized illumination. Blue and red curves show the percentage of power coupled toward the specular direction (s_0^-) and first diffraction order (s_1^-), respectively. (c) Calculated (solid black line), and measured (yellow circles) angular dispersion of the gradient surface for the ± 1 diffraction orders. The black lines correspond to the ideal surface in panel (a) and the yellow circles are analogous results measured at λ=700 nm for the fabricated sample, as measured in chapter 18. A and B correspond to the ideal retroreflection points where $\theta_{back} = -\theta_{in} = \pm 35.7$ degrees (Littrow configuration). Inside the highlighted gray region, the non-specular diffraction orders are evanescent.

As expected, 100% coupling efficiency at θ_0=35.7 degrees is calculated, *i.e.*, $|s_1^-|^2 = 1$. For this AOI, the metasurface operates in the Littrow configuration and the angle of reflection equals 35.7 degrees. In addition, Fig. 4 (a) shows that the angular response is considerably robust and, for an AOI range $11 < \theta_{in} < 80$ degrees, over half of the incident power is redirected into the non-specular direction, while the structure was not optimized for off-Littrow operation. This broad angular response is associated with the fact that the momentum imparted by the surface does not change with the incidence angle [5], and it is sufficiently negative to ensure that the angle of the emerging reflected beam stays negative over a very broad angular range. The back reflection angle varies as a function of impinging angle following the grating equation for first-order diffraction

$\theta_{retro} = \sin^{-1}(\sin\theta_{in} \pm \frac{\lambda}{\Lambda})$, where the sign refers to $\theta_{in} > 0$ and $\theta_{in} < 0$ respectively, as plotted in Fig. 4 (c). Yet, as expected, the scattered beam always lies in the same half-plane as the incident one. The lower cut-off for $\theta_{in} = 11$ degrees is simply determined by the cut-off of s_1^- for close-to-normal incidence, and it can be adjusted by design.
Following from reciprocity, the response of the back reflective surface has to be symmetric [27, 28] . This leads to an interesting feature of a symmetry evident in Fig. 4 (b) that arises despite the fact that its geometric profile, described by Eq. (10), is asymmetric and tailored for a specific oblique illumination. More specifically, if the surface is designed to retroreflect with unity efficiency for the AOI θ_0, it ensures zero coupling to the specular direction. Reciprocity then ensures that, when illuminating the surface from the specular direction, no power can be coupled back towards θ_0. Given that the period is unaffected by the incidence direction, and it is designed to admit only two diffraction orders, all energy will be coupled to the back reflected beam when excited from the specular direction. Likewise, and given the broad angular response in the negative half plane, reciprocity ensures an equally broad response for positive incidence angles.

2.4 Development of graded metasurface design

With the linear phase profile in Fig. 3 (b) and the approximately linear phase profile in Fig. 4 (a), the metasurface performance is expected to be robust to surface discretization. Given that surface discretization is necessary in practical designs, its effect on the retroreflective efficiency (*i.e.* in Littrow configuration) of the ideal surface studied in Fig. 4 is investigated. The metasurface is designed to fully retroreflect the incident wave for an incoming angle of $\theta_{in} = 35.7$ degrees at λ=700 nm. The required local reflection phase of this surface is shown in Fig. 5 (a) in black lines. Each period of the surface is then divided into N segments, and N is increased from 1 to 16. The case N=1 represents a fully homogeneous surface and the case N=16 is a finely discretized surface for which the length of each step is 605 nm/16=37.8 nm. For comparison, in Fig. 5 (a) the quantized reflection phase along the surface for the N=4 case is plotted as well. Implementing the new reflection coefficients based on the technique explained in chapter 2.3, the percentage of power coupled toward specular reflection and retroreflection is calculated numerically as function of N. The results are shown in Fig. 5 (b). As expected, for N=1 the surface is a simple mirror that imprints a constant phase onto the specularly reflected wave s_0^-. As the number of surface segments is increased, the first negative diffraction order s_1^- rapidly increases, and surprisingly for only two phase steps more than 75% of the incident power is already retroreflected. We note that in this case the metasurface is still symmetric but the excitation asymmetry enforces an asymmetric scattering from the surface. For N=3, which corresponds to our physically implemented surface in chapter 3.1, a 90% efficiency

in a lossless ultrathin structure is predicted. Quite interestingly, in experiments (Chapter 5) around 85% efficiency is obtained which is consistent with the amount of absorption from the back reflector (see Fig. 18). Beyond this level of discretization the retroreflection efficiency is more than 98%, confirming the robustness of its response to surface discretization. However, it should be noted that the implementation of N=2 discretization steps was realized in the same manner by placing only one TiO_x line per unit cell, and the predicted efficiency was exceeded and reaches similar values as the N=3 design. This is discussed in more detail in chapter 4.2.2 and 5.3.5.

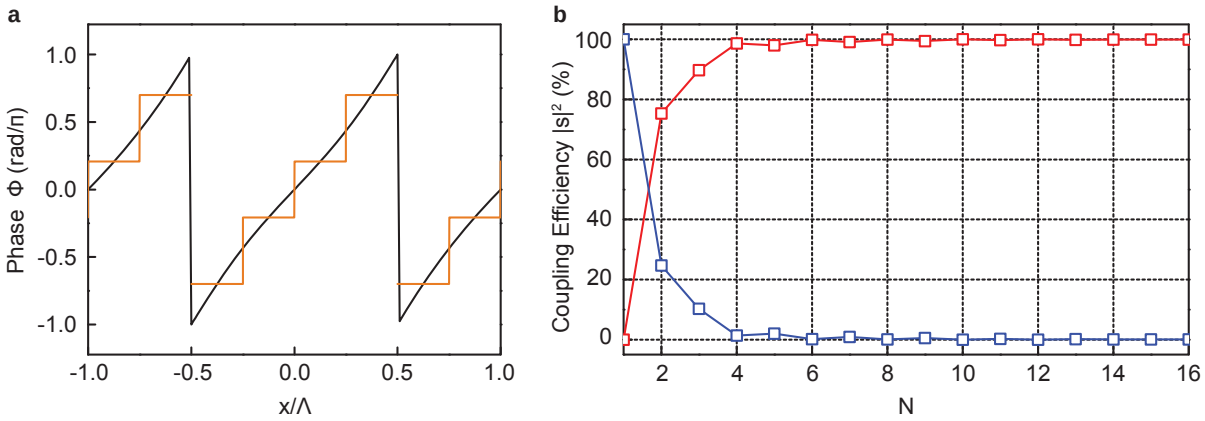

Figure 5: Discretized local reflection and effects of surface discretization (a) Calculated ideal local phase profile of the surface $\Phi(x) = \angle r(x)$, designed for an incoming angle of $\theta_{in} = 35.7$ degrees (black line), and the discretized reflection profile for N=4 (purple line). The surface period is Λ=605 nm for operation at λ=700 nm. (b) Coupling efficiency of the surface when the ideal continuous profile is discretized into N steps. Blue and red lines correspond to the numerically calculated coupling efficiency for an incident s-polarized wave at $\theta_{in} = 35.7$ degrees, reflecting toward the specular direction (s_0^-) and retroreflection (s_1^-), respectively.

The reason behind this robustness is again associated with the nature of our design. First, the diffraction phenomenon is non-resonant and therefore insensitive to perturbations. Second, the period Λ determines two propagating diffraction orders for the operational frequency, ensuring that, as long as the overall phase gradient along each unit cell suppresses the coupling towards the zero-th order (specular) diffraction, reflection will be funneled towards the first order in the back direction. The fabrication of the structure with the phase profile discretized into N=3 steps is decried in the next chapter.

3 Experimental realization of graded metasurface

3.1 Assymetric grating with graded effective index

The device characterized in the next chapter was realized using a nanostructured dielectric metasurface with subwavelength thickness, made of TiO_x rods on top of a protected Ag mirror. The dielectric nature of TiO_x, and its relatively high index ($n = 2.35 + 0.01i$ for λ=500 nm to $n = 2.23 + 0.01i$ for λ=1000 nm, see appendix A.1), are suitable to minimize absorption and provide enhanced phase control over an ultrathin thickness.

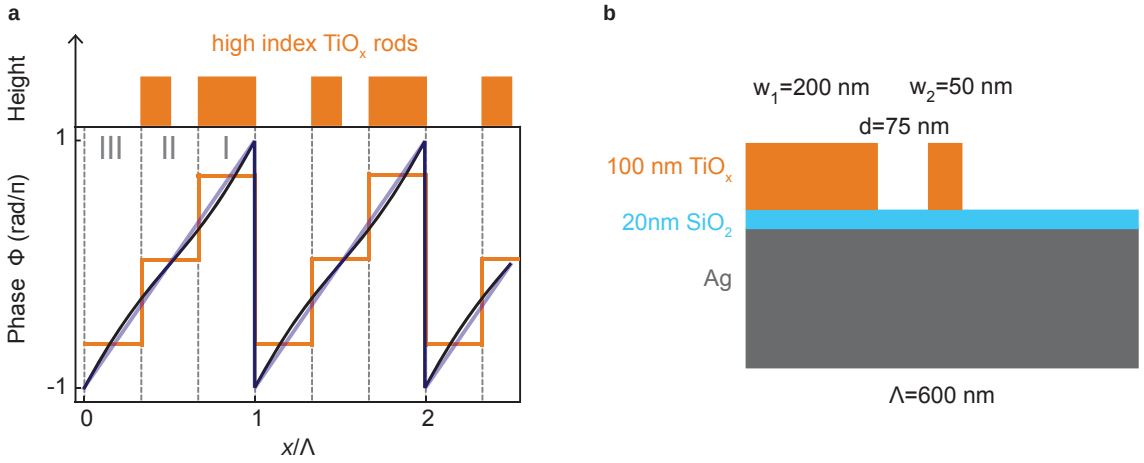

Figure 6: Realization of surface phase discretization by asymmetric grating (a) Schematic of development of structure geometry. The ideal phase profile derived from the generalized law of reflection (blue transparent line) and from the Huygens'-Fresnel principle (black solid line) are similar in shape. The profile is discretized in N=3 discretization steps. The effective index of each discretization element is controlled by adjusting the geometry of high-index TiO_x rods or by employing the bare back mirror. This leads to a design of an asymmetric grating of TiO_x nanorods on top of the Ag mirror. (b) Initial ideal design of a unit cell of the asymmetric grating of TiO_x rods on top of a protected Ag mirror. The unit cell with a length of 600 nm is optimized for λ=850 nm at an AOI of θ_{in}=45 degrees.

At first, the structure was designed with three phase discretization steps per unit cell, N=3, for operation at λ=850 nm, tailored for s-polarized excitation. The phase variation of the local reflection coefficient in the three elements is achieved by controlling the effective index of each element. By this, in each element the light will experience a different phase shift as the wavevector k depends on the refractive index n:

$$k = \frac{2\pi}{\lambda} = \frac{2\pi n}{\lambda_0} \tag{11}$$

Here, λ_0 is the wavelength in free space. k is the spatial derivative of the phase:

$$\frac{\Phi}{dz} = k \tag{12}$$

meaning that k describes a change in phase with change of position [29].
The effective index and therefore the phase variation of the local reflection coefficient in the first two segments is achieved by controlling the width of the nanorods, so that the required reflection phase is imparted over the width of one segment. For the third segment the bare back-mirror is employed and with the refractive index of air n=1 no additional phase shift is imprinted onto the reflected light here. The schematic of realizing the phaseshift via an asymmetric grating structure is shown in Fig. 6 (a). The initial outline for the unit cell of an ideal discretized design therefore consisted of two rectangular TiO_x with the same height but different width on top of an Ag mirror, as shown in Fig. 6 (b). Simulations using the finite-element method for determination of optimized parameters have been performed initially to find an ideal design for operation at λ=850 nm and AOI θ_{in}=45 degrees as it is shown in the figure. The SiO_x layer prevents losses due avoidance of the creation of surface plasmons and the ideal thickness was determined to be between 20-25 nm. In this optimization routines it has been found that the design of the structure is robust against variation, for example changing the shape of the nanorods from rectangular to trapezoidal, decreasing the height of the thinner rod or increasing the gap size d between the two TiO_x rods does not influence the overall performance of the structure crucially. In the final fabrication results, the shape of the TiO_x rods are trapezoidal and of different height due to the evaporation process and the gap d between the two rods was widened compared to the ideal design to simplify the nano-fabrication process. Details can be found in the following description of the fabrication process. Initially designed with a period of Λ=600 nm for ideal performance at λ=850 nm, the final structure has a period of λ= 605 nm, and is therefore optimal for retroreflection at a wavelength of λ=750 nm and an AOI of θ=35.7 degrees.
The metasurface was fabricated by two different methods, namely top down and bottom up fabrication, using e-beam lithography, evaporation and reactive ion etching (RIE etching). As described in the following, both methods posed a challenge in realizing the initial ideal design. The bottom up fabrication was finally chosen and led to an adequate sample on which optical experiments could be performed successfully.

3.2 Bottom up technique

3.2.1 Bottom up fabrication of graded metasurface

The different steps of the bottom up fabrication are depicted in Fig. 7. A 1-mm-thick Si wafer was cleaned by base piranha and coated with 1-2 nm Ge (evaporation rate: 0.1 Å/s) as a seed layer followed by 200 nm of Ag (1.8 Å/s) and 20-30 nm of SiO_x (0.2 Å/s) using thermal evaporation at a pressure of 10^{-6} mbar. On this protected mirror a 12 s

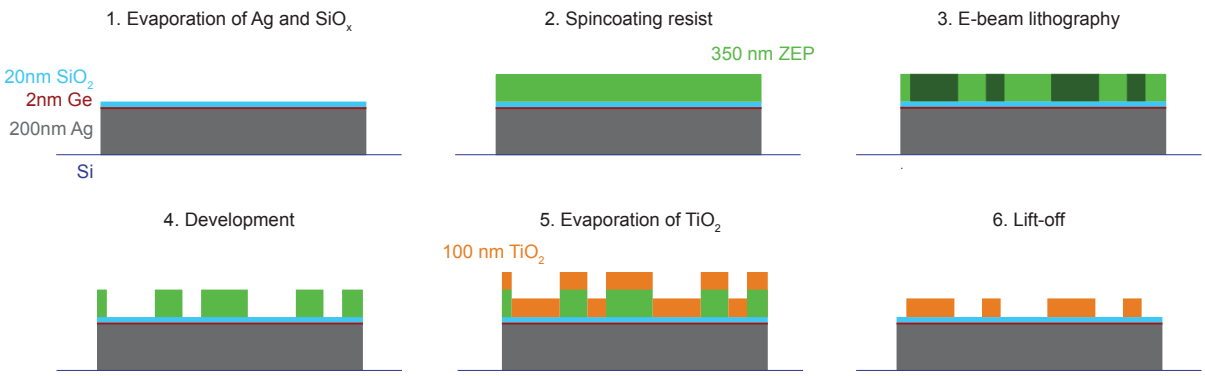

Figure 7: Bottom up fabrication steps 1. Thermal evaporation of 1-2nm Ge, 200 nm Ag and 20-30 nm SiO_x on top of a 1-mm-thick Si wafer. 2. Spin-coating of 350-360 nm of negative tone resist ZEP520a and Espacer 300z on the protective mirror. 3. Patterning of the structure into the ZEP layer by E-beam lithography. 4. Development of the activated resist layer in Pentyl Acetate resulting in the inverse pattern in the resist, followed by critical point drying. 5. E-beam evaporation of 100nm TiO_xon the patterned resist. 6. Lift-off in ultrasonic bath in Anisole.

O_2 descum RIE plasma etch (see RIE etch recipes in table 1) was applied to clean the sample and to make it hydrophilic. Then, the wafer was spin-coated at 1500 rpm for 45 seconds with ZEP520a, a high-resolution positive tone resist, and postbaked for 5 minutes at 180 °C. The resist layer had a thickness of 350-360 nm. Next, Espacer 300z was spin-coated at 2000 rpm for 45 seconds to improve the conductivity of the sample, dried for 2 minutes at room temperature and then baked for 5 minutes at 110 °C. The asymmetric grating was written by e-beam lithography using a 20 keV beam, an aperture of 10 µm and a dose of 50 $\mu C/cm^2$. The patterned area was 1.5 × 1.5 mm^2, comprised of stitched 100×100 μm^2 write fields. Afterwards the sample was rinsed 30 seconds in water to remove the espacer and developed in Pentyl Acetate for 45 seconds, rinsed 15 seconds in a mixture of methyl isobutyl ketone and isopropanol (MIBK:IPA,9:1), dipped into IPA and transferred to ethanol. To prevent collapse of the fragile resist patterns the sample was dried at the critical point. The lines were then filled with 100 nm of TiO_x by e-beam evaporation (rate: 0.5 Å/s) at a pressure of $7x10^{-6}$ mbar. Lift-off was done by dissolving the resist for 10-12 minutes in an ultrasonic bath in anisole, followed by a rinse in IPA.
Optical measurements were carried out on the sample, fabricated by the described bottom up fabrication and are reported in chapter 5. The geometry of this structure was used for simulation of the coupling efficiency as descirbed in chapter 4.
A tilted top image and a cross section image of this structure, taken by a scanning electron microscope (SEM), are shown in Fig. 8. As it can be seen in these images the final rods have a trapezoidal shape and the rod with the smaller width is also lower than the rod with the larger width. This is due to the fact that during the evaporation of

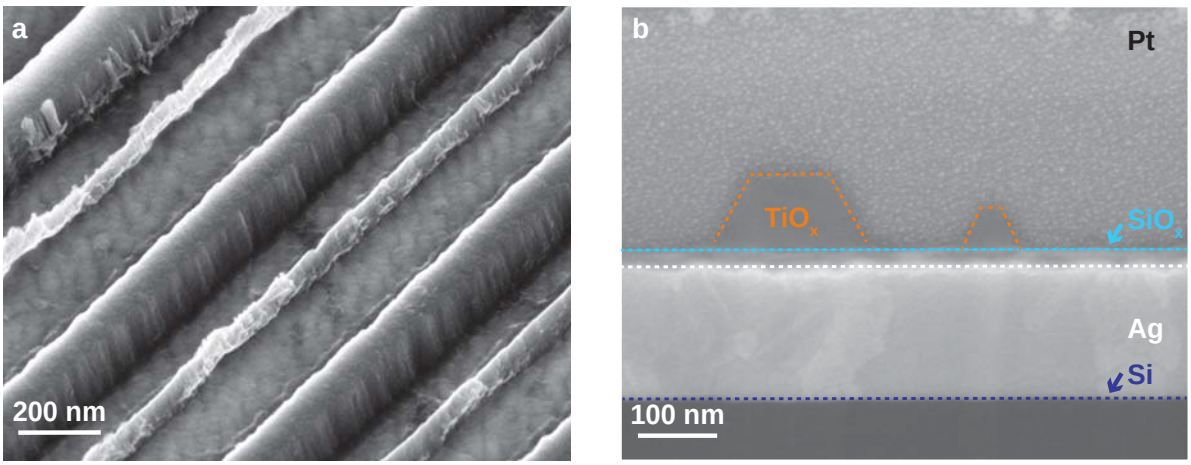

Figure 8: SEM image of tilted top view and cross section of sample from bottom up fabrication (a) SEM image of structure fabricated with bottom up technique under tilt of 40 °. (b) FIB cross section of the same sample. Depicted is unit cell with a tall and a low TiO_x rod. The dashed lines indicate the borders between the different materials. Pt on top of the structure is needed to get clean cross sections and evaporated before the milling process.

TiO_x the upper edges of the pattern in the resist are slowly covered by TiO_x, so that the sides of the gaps cannot be filled up with TiO_x. In the case of the lower rod, the aspect ratio of the gap is so high that an evaporation of 100 nm TiO_x is not possible before the upper side of the gap is completely covered with a layer of TiO_x and does not enable further growing of the rod. A possible solution to get two rods of the same height with the bottom up fabrication could be a milling step during the evaporation process to remove the TiO_x cover on top of the resist. However, the structure with this dimensions represents an adequate discretization of the unit cell, as the calculated optical response and the optical simulations show good overlap (See chapter 2.3 and chapter 5).
Completed dimensions were measured using a focused ion beam (FIB, FEI Helios Nanolab 600) to cut cross sections, with dimensions measured by electron micrographs. The metasurface consisted of two trapezoidal rods repeating in unit cells with a periodicity of 605 nm. The taller line had a height of 100 nm, a bottom width of 180 nm and a top width of 100 nm. The narrower line, separated from the tall line by a gap of 120 nm, had a height of 50 nm with bottom and top widths of 60 nm and 20 nm respectively.

3.2.2 Challenges of bottom up fabrication

Fabricating two elements with different geometries at the same time is challenging in nano-fabrication as processes have to be optimized for both elements. The main difficulty during the bottom up fabrication process was to achieve a stable resist pattern after development. Due to the high aspect ratio of the remaining resist pillar between the

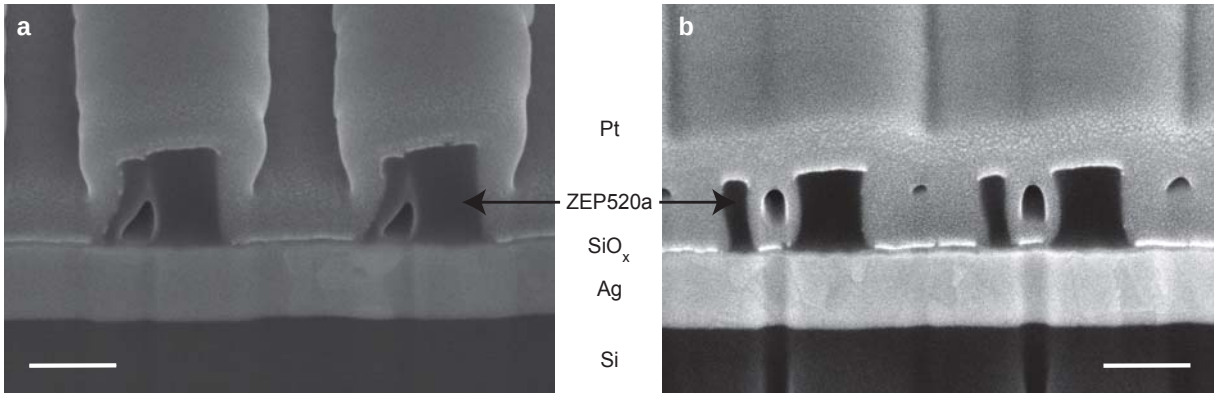

Figure 9: SEM images of cross sections of structure after developing for different times Protective mirror (Ag+SiO_x) on Si with resist (ZEP520a) lines that form the inverse pattern of the ultimate structure. The progress corresponds to the structure after step 4 in Fig. 7. The structure is covered with a layer of Pt for making clean cross sections. Both samples have been patterned by e-beam lithography with a dose of 45 µC/cm^2 and developed for (a) 60 seconds and (b) 45 seconds. Scale bar is 200 nm.

wide and the narrow gap, this pillar tends to collapse. The electron dose as well as the developing time were varied to achieve stable resist patterns with the right geometry. Besides that, the sample was dried at the critical point after development to prevent a resist collapse due to surface tension. In Fig. 9 two cross sections of the inverse resist pattern of two samples with the same dose but different developing times after developing and before TiO_x evaporation are shown. While Fig. 9 (a) shows a collapse of the middle pillar after developing for 60 seconds in Fig. 9 (b) a stable pattern can be seen after developing for 45 second. Hence, in the fabrication process a developing time of 45 seconds was chosen.

3.3 Top down technique

3.3.1 Top down fabrication of graded metasurface

As described in the previous chapter the bottom up fabrication leads to trapezoidal rods of different height. In order to achieve the intended structure of two rectangular rods of the same height (as shown in Fig. 6 (b)), samples following the top down method were fabricated. However, the process has not been optimized during this project, and the fabrication of the structure that is closest to the intended geometry is described here.

The different steps of the top down fabrication method are depicted in Fig. 10. In the same manner as described for the bottom up fabrication, a Si wafer was cleaned and coated with Ge, Ag and SiO_x and 100 nm TiO_x was evaporated directly on the protective mirror with the same rates as noted above. After 12 seconds of O_2 descum, the wafer was

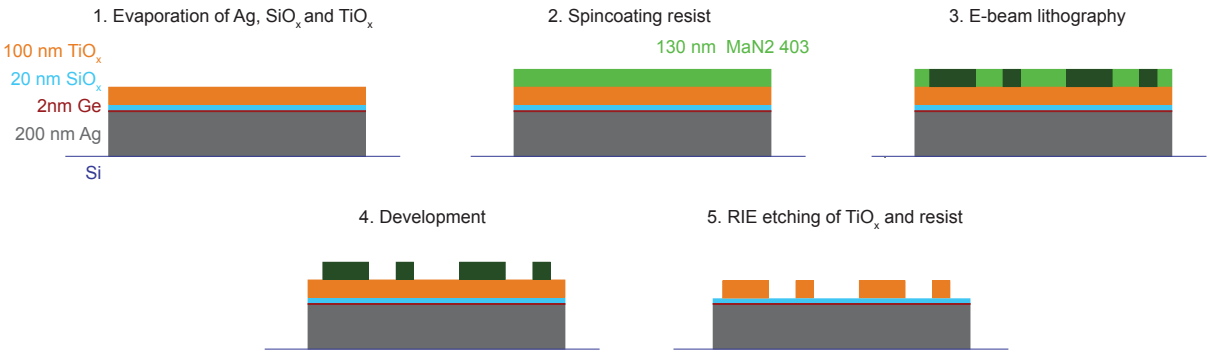

Figure 10: Top down fabrication steps 1. Thermal evaporation of 1-2 nm Ge, 200 nm Ag and 20-30 nm SiO_x and e-beam evaporation of 100 nm TiO_x on top of a 1-mm-thick Si wafer. 2. Spin-coating of 130-140 nm of negative tone resist MaN2403 and Espacer 300z on the TiO_x. 3. Patterning of the structure into the resist layer by E-beam lithography. 4. Developing the activated resist layer in MaD525. 5. RIE etching of the substrate to transfer the pattern of the resist into the TiO_x layer.

spin-coated with the negative tone resist MaN2403 at 2800 rpm for 45 seconds to form a 130 nm thick layer, and baked for 4 minutes at 90 °C. Again, Espacer 300z was spincoated for an improved conductivity. The resist was patterned using E-beam lithography with a 30 keV beam, an aperture of 10 µm and a dose of 130 µC/cm^2. The patterned area was 1.5 × 1.5 mm^2, comprised of stitched 100×100 µm^2 write fields. Further, the sample was rinsed 30 seconds in water, developed in constantly stirred MaD525 for 3 minutes and rinsed twice in water for 15 seconds. After hardbaking of the sample at 115 °C for 90 seconds, the pattern was transferred from the resist into the TiO_x by RIE etching using the TiO_x etch recipe 1, as described in Tab. 2. The sample was etched for 4 minutes. After that time the resist was nearly gone. An additional O_2 descum step could remove the residual resist, but has not been performed here.

SEM images of the topview and of the cross section of the sample are shown in Fig. 11. In both figures it can be seen that the lines are narrow compared to the initially intended design, especially the smaller rod that has only a width w_2 of 20 nm, which might be as the chosen dose for the e-beam writing was to small. In further steps different doses for the wide and the narrow lines have been tried. In the cross section in Fig. 11 (b) it is seen that the TiO_x layer in the small gaps between the lines is not etched as far as the TiO_x layer in the wide gaps. Further optimization of the e-beam lithography parameters as well as the etching recipes is needed for successfully usage of the top down fabrication method.

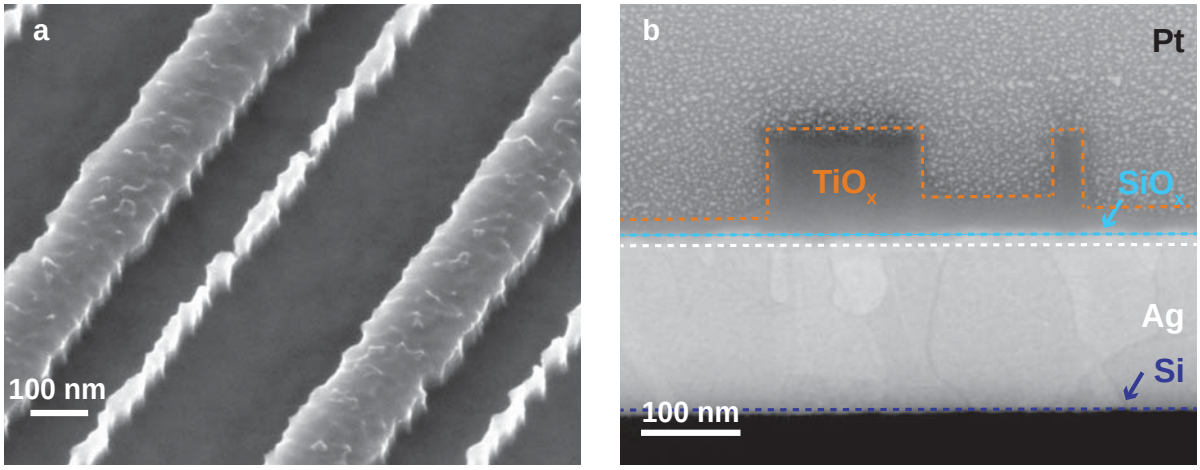

Figure 11: SEM image of tilted top view and cross section of sample from top down fabrication (a) SEM image of structure fabricated with top down technique under tilt of 40 degrees. (b) FIB cross section of the same sample. Depicted is one unit cell with a wide and a narrow TiO_x rod. The dashed lines indicate the borders between the different materials. Pt on top of the structure is needed to get clean cross sections and evaporated before the milling process.

3.3.2 Challenges of TiO_x RIE etching

The challenge of the top down method arises in particular from finding an etch recipe that etches TiO_x anisotropically. Due to the high aspect ratio of the structure, a good etch selectivity between the mask and the TiO_x is needed. Earlier the E-beam resist HSQ and metal nanomasks consisting of Cr has been reported as etching masks with good selectivity [30]. However, the usage of these materials for masking was not tried in this fabrication process as removing the mask (e.g. by wet etching) from the final structure would be a complicated process that might damage the sample. By using a mask of the e-beam resist MaN2403, the selectivity of the etching process has been determined to be below 1 and therefore so low that the thickness of the mask should be higher than the thickness TiO_x layer. At the same time, the usage of CF_4/Ar plasma for TiO_x etching like reported elsewhere [30, 31], was not possible as CF_4 was not available in the plasma etcher system. Applying different materials for masking and optimal chemicals for RIE etching could be investigated in more detail in future projects to obtain improved etching results.

While trying to find etching parameters which lead to improved results in particular the role of a small part of O_2 in the plasma etching has been studied. In Fig. 12 two samples are shown that were fabricated with the same lithography parameters (dose for wide line: 150 µC/cm^2, dose for narrow line: 180 µC/cm^2) but etched either with the TiO_x etch recipe 1 or 2 (see table 2), with the difference that TiO_x etch recipe 1 does contain a

Parameter	O_2 descum
O_2 flow	25 sccm
Pressure	5 mTorr
Strike pressure	10 mTorr
ICP forwards power	50 W
Temperature	20°C

Table 1: Parameter of RIE Plasma etching recipes for O_2 desum

Parameter	TiO_x etch 1	TiO_x etch 2
CHF_3 flow	25 sccm	25 sccm
Ar flow	25 sccm	25 sccm
O_2 flow	2 sccm	-
Pressure	30 mTorr	30 mTorr
ICP forward power	300 W	300 W
Temperature	20°C	20°C

Table 2: Parameter of RIE Plasma etching recipes for TiO_x etch. TiO_x etch recipe 1 without and TiO_x etch recipe 2 with O_2 part.

small part of O_2 but TiO_x etch recipe 2 is free from O_2. Comparing the cross sections in Fig. 12 (a) and (b), a white protective layer, that might be comprised of Teflon [32], was formed during the etch and is visible in (b) for the sample with a recipe without O_2. In this case the formation of a protective layer on the edges of the rods is not beneficial but leads to a deformation of the structure dimension. It is known that O_2 in the plasma suppresses the formation of a protective layer during the etch [33]. In the cross section images it is also visible that the resist mask is removed before the TiO_x layer is etched until the bottom due to the small selectivity.

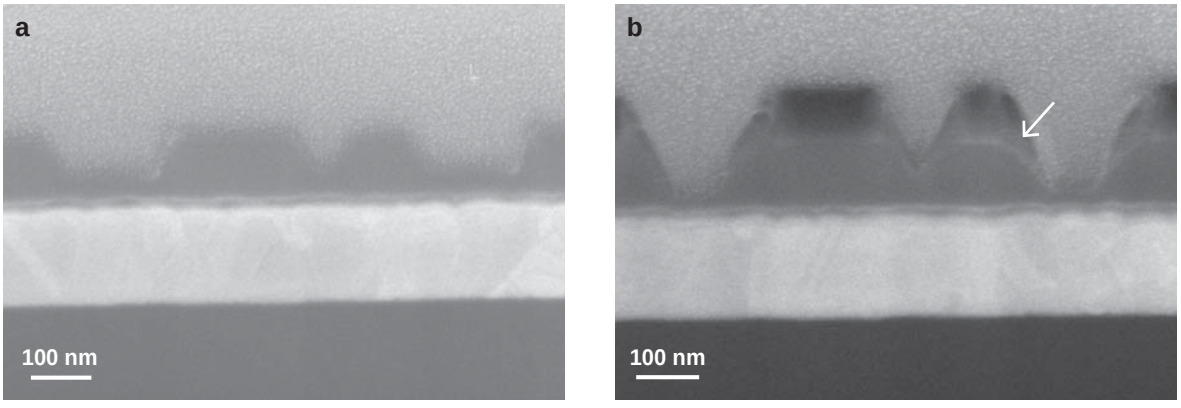

Figure 12: SEM image of cross section of sample from top down fabrication Cross section of sample fabricated with top down technique with (a) RIE etching with TiO_x etch recipe 1 for 6 minutes. (b) TiO_x etch recipe 2 for 5,5 minutes. Etch recipes are listed in table 2. A white protective layer, that is probably a Teflon-like film, is formed on the edges of the rods during etching (indicated by white arrow).

4 FEM and FDTD modeling of metasurface back reflector

4.1 Simulation methods

In this chapter the coupling efficiency to the specular order (s_0^-) and the first negative diffraction order (s_1^-) of a structure with the fabricated geometry was calculated. The asymmetric design does not allow to derive the coupling efficiency analytically. Hence, electromagnetic (EM) simulations have been performed in this project for finding numerically approximate solutions of the Maxwell's equations.

Two different EM simulation techniques, the finite-element (FEM) and the Finite-difference time-domain (FDTD) method have been used [34, 35]. In both methods the physical problem is spatially discretized into a meshgrid and for each mesh element the field that satisfies the boundary condition is found. The solution process is different for the methods. FEM solves in frequency domain and directly determines local functions of each mesh element by finding the solution of one matrix. In FDTD also the time is discretized in time steps, a plane wave starts at an initial time and the solutions of each mesh cell are found in an iterative process. A Fourier transformation of the solution in time domain determines the optical response in frequency domain.

First, numerical simulations were carried out by the 2D FEM software COMSOL Multiphysics in the frequency-domain radio-frequency module and second 2D FDTD simulations were performed using Lumerical FDTD software.

The FEM simulations have been performed by Nasim Mohammadi Estakhri and are used to model the ideal retroreflector characterized in Fig. 4 as well as the fabricated device which was used to perform the optical measurements. The FDTD simulations were carried out only for modeling the fabricated device. This was done to confirm the solutions of the FEM simulations for the structure with N=3 discretization steps, and to simulate the response of the fabricated structure with N=2 disretization steps.

4.1.1 Frequency-domain modeling by FEM

In the simulations performed with FEM, periodic ports and Floquet periodicity boundary conditions are used to model one unit-cell of each metasurface. Ports are placed far enough from the metasurface such that all evanescent scattering modes are sufficiently weak to not influence the result.

The surface profile for the ideal retroreflector characterized in Fig. 4 is modeled as a sheet admittance, with $h = \lambda/20$=35 nm for the distance between the sheet admittance $Y_{surface}$ and the ground plane. In general, the relation between the local phase and the

admittance reads:

$$\eta_0 Y_{surface} = -i \tan\left(\frac{\Phi(x)}{2}\right) + i \cot k_0 h \tag{13}$$

where $\Phi(x) = \angle r(x)$ and η_0 is the free-space characteristic impedance. Substrate and free space are meshed with maximum element sizes of 2 nm and 26 nm, respectively. Perfect electric conductors are used in the ideal retroreflector set up.

To model the fabricated device, the SEM images in Fig. 8 were used and dimensions estimated as described in the fabrication process in chapter 3.1. All materials are modeled as dispersive and lossy and realistic values for the permittivities of silver and SiO_2 are used from experimentally retrieved data sets [36, 37]. For TiO_x, the refractive index was measured for a sample of TiO_x on a Si wafer by spectroscopic ellipsometry and values between n=2.35 for λ=500 nm and n=2.23 for λ=1000 nm are determined. A short description of the ellipsometry technique and the determined dielectric index of TiO_x (Fig. A1) is shown in the appendix. Maximum element size of 20 nm is used for high-index TiO_x rods and the remaining parts are meshed with maximum element size of 28 nm. A silver layer with thickness of 200 nm is used as the back reflector which is truncated with perfectly matched layer to model a semi-infinite ground plane. The scattering parameters of the port are used to calculate the percentage of the power coupled toward each channel. The results of the simulations for the fabricated device can be found in chapter 5 for direct comparison next to the respective measurement results. The results of the angular/wavelength dispersion of the structure for the angular range θ_0=0 - 85 degrees and the wavelength range 450-1000 nm is shown in Fig. 15, next to similar simulations performed by FDTD.

4.1.2 Time-domain modeling by FDTD

FDTD simulations, using the Lumerical FDTD software, were performed in addition to the FEM simulations. A periodic array with a unit cell of Λ=605 nm was simulated using the Broadband Fixed Angle Source Technique (BFAST). BFAST allows to calculate the response of a periodic structure at oblique incidence for a wide band of wavelengths [38]. By using BFAST, the boundary conditions transverse to the wave propagation are automatically set to periodic boundary conditions based on BFAST's formulation. For the boundary conditions in horizontal direction of the structure metal boundary conditions were used in the silver layer to mimic a infinite thick silver mirror and stretched coordinate perfect matched layers (PMLs) with a steep angle profile were used to simulate the air above the structure. A broadband (450-1000 nm) BFAST s-polarized plane wave was injected between 0-74 degrees from the top and the reflected power from the metasurface was monitored. A far-field transformation routine was used to determine the power of each

diffraction order. The structure with N=3 discretization steps had the same dimensions as in the FEM simulations, determined from the SEM cross-section image of the sample. Additionally, simulations with the same settings, but removing the smaller TiO_x bar for a structure with N=2 discretization steps have been performed. For the simulations a unform 7 nm mesh, with a 4.5 nm refinement mesh around the TiO_x structures was chosen. The optical constants for Ag and SiO_2 were taken from a Drude-Lorentz model fitted to the data from Palik [39]. For TiO_x the self measured optical data as described before was used. Converging tests has been performed for an incoming angle of 35.7 degrees. The simulation could kept stable for oblique angles up to 74 degrees with the same simulations settings used for all angles. Results of the FDTD simulations are shown in Fig. 13 - 15.

4.2 Modeling of optical response of graded metasurface

4.2.1 Coupling efficiencies at different wavelengths

In Fig. 13 the angular response of the structure with N=3 discretization steps is calculated for λ=700 nm, λ=750 nm and λ=850 nm. At the ideal wavelength of 700 nm for which the structure was designed, coupling efficiency towards the first negative diffraction order s_1^- above 90 % is reached for a broad band of angles from θ_{in}= 15-65 degrees (red curves in Fig. 13). This result matches the results obtained with FEM and by optical measurements (see Fig. 18). With shifting the wavelength toward the infrared, the coupling efficiency for back reflection is decreasing as can be seen in Fig. 13 (b) and (c) for λ=750 nm and λ=850 nm, respectively. However, this strong reduction of the coupling efficiency is neither observed at FEM modeling nor in the optical measurements of this wavelength, where only a minor decrease in coupling efficiency is determined. The lower cut-off angles which is caused by the grating nature of the structure match in both simulation methods as well as in the measurements for all three wavelengths. The upper cut-off angle is not determined with FDTD as using this method the simulation could only be kept stable until angles up to 74 degree. Finally, a clear difference in the coupling efficiency towards the specular order s_0^- for angles between the positive and negative inner cut-off angles emerges in the two different simulation methods. Higher efficiency were obtained with FDTD than with FEM which matches with the measured efficiency.

It can be concluded that the FEM and the FDTD simulations of the angular dispersion show the same trend with minor disparities in the strength of the coupling efficiency toward the specular and the first negative diffraction order. The reasons for this disparity lies naturally in the usage of two distinct EM simulation techniques.

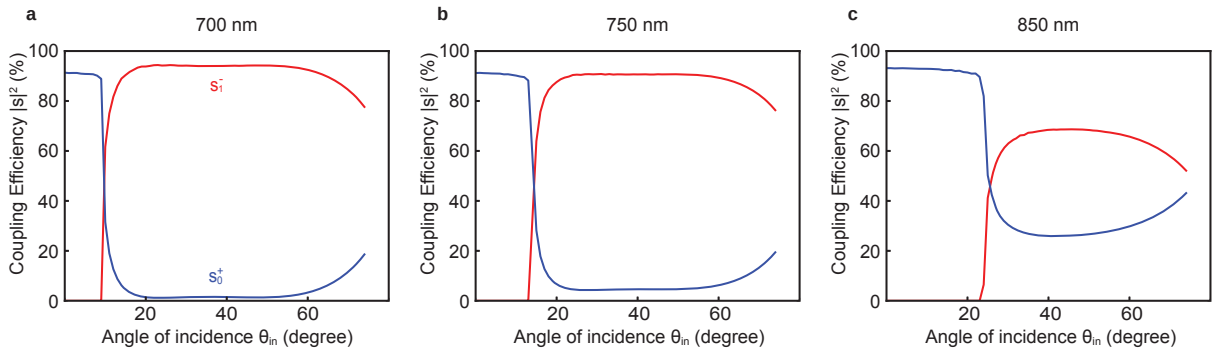

Figure 13: Angular response of structure with fabricated dimensions for different wavelengths Comparison of FDTD-simulated angular dispersion of the fabricated structure at wavelengths of (a) λ=700 nm (b) λ=750 nm and (c) λ=850 nm. The specular reflection (s_0^-, blue solid line) and the back reflection (s_1^-, red solid line) is shown.

4.2.2 Coupling efficiency for N=2 and N=3 discretization

Next, the coupling efficiency for a structure with one TiO_x line was simulated to mime a discretization to N=2 phase regions, following the approach described later in chapter 5.3.5. A decrease in efficiency of the back reflection to 75% as calculated in chapter 2.4 is expected in comparison with the structure with two TiO_x lines. However simulations do not show a reduction in coupling efficiency if only one TiO_x rod is placed on the surface, but a minor increase in efficiency for angles between θ_{in}=21-51 degrees (See Fig. 14, solid lines). For the structure with N=3 discretization steps (Fig. 14, dashed lines), the coupling efficiency is slightly lower in these region, however, the coupling functionality is efficient up to higher incident angles. The same trend can be observed in optical measurements and is discussed in chapter 5.3.5.

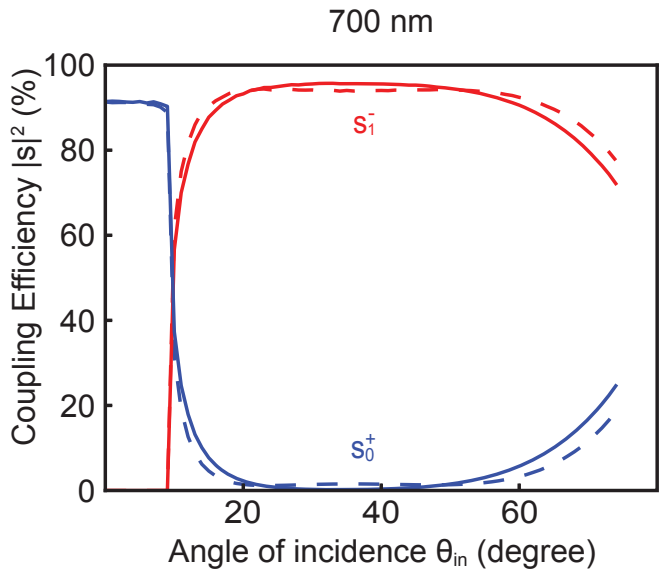

Figure 14: Angular dispersion of structure with fabricated dimensions with N=2 and N=3 discretization steps. Coupling efficiency, calculated by FDTD, of λ=700 nm toward the specular order s_0^- (blue) and the first negative diffraction order s_1^- (red) is shown for the structure with one (solid lines) and two TiO_x rods per unit cell (dashed lines).

4.2.3 Angular/wavelength dispersion

The angular dispersion for the structure with N=3 discretization steps, meaning two TiO_x line, was performed for wavelengths between λ=450 nm-1000 nm for incoming angles θ_{in}=0-85 degrees (FEM) and θ_{in}=0-74 degrees (FDTD) to show that the coupling toward the first negative diffraction order is efficicient for a broad band of wavelengths and a wide range of incident angles. Simulation results of the fabricated design with N=3 discretization steps is depicted in 15 (a) and (b) for modeling with FEM and FDTD, respectively, and the 75%-power and 50%-power operation regions are highlighted. More than 50% back reflection is achieved across λ=490-940 nm and θ_{in}=24-51 degrees in FEM simulations. With FDTD a similar result is obtained, however the bandwidth of 50% back reflection is reduced to only λ=490-900 nm and θ_{in}=24-51 degrees. As mentioned before, the different simulation results are based on the usage of distinct simulation methods as well as using different simulation parameters. However, the trend of the results obtained by using the different methods are clearly obtained and lies in the expected deviation.
Finally, the the angular/wavelength dispersion for a structure with the geometry of a design with N=2 discretization steps, and therefore one TiO_x line was calculated (FDTD). The angle range of efficient back reflection is decreased compared N=3. More than 50% back reflection is achieved across λ=490-900 nm and θ_{in}=24-40 degrees. Using only one instead of two TiO_x lines is reducing the angle range of efficient coupling toward the first negative diffraction order and confirms the finding of the previous chapter (Chapter 4.2.2). Still, the performance of the structure is efficient for a broad range of wavelength and angles.

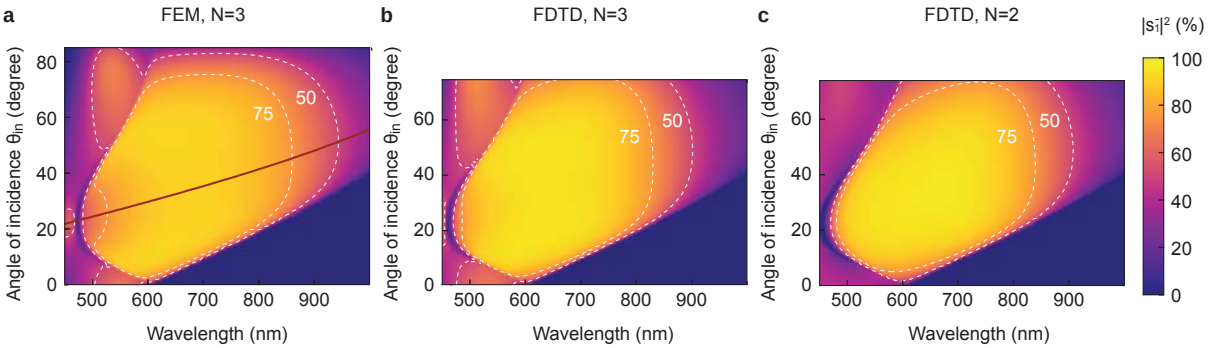

Figure 15: Angular/wavelength dispersion of the structure with the fabricated dimensions Coupling efficiency toward the first-order negative reflection s_1^- with highlighting of the 75%-power and 50%-power operation regions (white dashed lines). (a) Angular/wavelength dispersion of fabricated design with N=3 discretization steps (FEM). The dark red line indicates the retroreflective loci, for which the incoming and the reflected wave are aligned ($\theta_{out} = -\theta_{in}$). (b) Angular/wavelength dispersion of fabricated design with N=3 discretization steps (FDTD). (c) Angular/wavelength dispersion of fabricated design with N=2 discretization steps (FDTD).

5 Optical measurements on metasurface back reflector

5.1 Optical visualization of back reflection

Before performing quantified optical measurements, the functionality of the structure has been imaged by photographs of the sample under illumination from different directions with a flashlight. Fig. 16 (a) - (c) visualizes the first order diffraction and specular reflection efficiency of the fabricated sample from the practical observer standpoint. The photographs of the samples can be seen below the schematic of the photography setup. In Fig. 16 (a) the bright specular reflection of the Ag mirror around the structure is visible while the dark square in the middle of the sample where the grating is placed indicates that specular reflection is almost absent. Even more, the bare absorptive Si area on the lower right side of the sample which stays uncovered during the fabrication process shows a reflection of blue light, which is typical for Si, while the back-reflective part in the middle of the sample is clearly darker than the silicon. In contrast, the center of the sample is noticeably bright for an observer sitting close to the excitation source, as can be seen in Fig. 16 (b)-(c) for different incoming angles. The Ag mirror and the Si area that surround the structure do not show any reflection at this position of perception. The bright color that can be observed in the diffraction reflection depends on the angle of observation and illumination.

5.2 Optical measurement setup: Rotating stage

To quantify the back reflection functionality of the fabricated device, the coupling efficiency to the two diffraction orders was measured experimentally using a rotating stage setup (See schematic of the measurement setup in Fig. 17 (a)). The sample was mounted in the center and the power meter on the outer ring of the rotating stage, while the illumination direction was held constant. This enabled independent control of excitation angles θ_{in} and sampling angles θ_{spec} for specular reflection and θ_{back} for the first negative diffraction order. We sweep the angle of the incident plane wave across $\theta_{in} = -80°$ to $\theta_{in} = 80°$. Thereby, the intensity of the scattered power for the allowed scattering modes s_0^- and s_1^- is measured. The structure was excited with a weakly converging beam to allow a well-defined excitation angle, and the reflected intensity to the specular and the first negative diffraction order was measured using an optical power meter (Powermeter PM100USB with Photodiode Power Sensor S121C (Thorlabs)). The reflected beam was focused on the power sensor, using a focusing lens (f=50 mm). All optical elements used in these setup were B-coated that means coated with a dielectric anti-reflection coat-

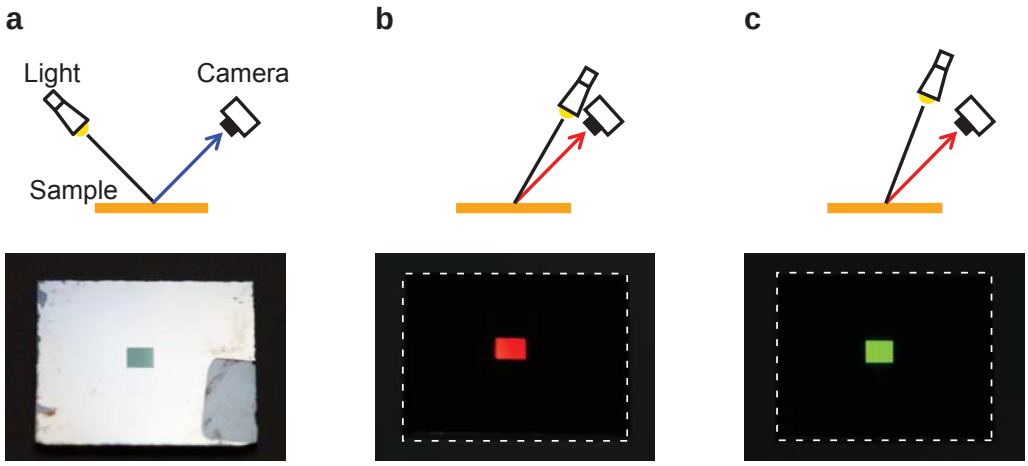

Figure 16: Optical visualization of back-reflecting effect Photographs of the fabricated structure on the bottom (1.5 x 1.5 mm^2 square in the center of 12 x 12 mm^2 silver mirror, bare Si residual from fabrication process in left lower corner) and schematic of photography setup on top row. (a) Specular response under illumination from the back with a commercial flashlight: observing no reflection in the specular direction from the structure (dark square in the middle). (b)-(c) Back reflective response of the sample when illuminated with a flashlight for different angles. The angle between light and camera was increased in (c) compared to (b).

ing that is optimized to minimal reflection in the wavelength range 600 - 1050 nm. By measuring the total beam power, the absolute reflectance was determined. Illumination and detection planes are slightly tilted vertically to allow back reflection measurements without blocking the incident light. Two different light sources have been applied for illumination.

In the first part of the project (Chapter 5.3.1, 5.3.2, 5.3.3, 5.3.5) a broadband laser-driven light source (LDLS) (EQ-99X, Energetiq) has been used. The schematic of this beam bath is shown in Fig. 1 (b). The light was coupled to a 50 µm core optical fiber by two parabolic mirrors with the end of the fiber on a fixed position in front of the rotating stage. The beam coming from the fiber was collimated with a lens (f=19 mm), send through a linear polarizer and focused with another lens (f=20 mm) on the surface of the sample. The focal point on the sample had a diameter of 0.75 mm. From this follows, that for excitation under an angle below 60° the focus was smaller than the structure with an area of 1.5 x 1.5 mm^2. Therefore, for measurements above this angle the light beam did not hit the structure solely but also the bare mirror substrate next to the sample. The measured intensities of specular and first order reflection did therefore not only depict the response of the structure, but the mixed reflection of structure and mirror. As the illumination source was broadband but the angular dispersion of a specific wavelength was of interest, optical filter (700 nm, 750 nm or 850 nm center wavelength, 40 nm bandwidth, Andover

Corporation) for the particular wavelength was placed in front of the power sensor.

For the second part of the project (Chapter 5.3.4), the broadband light source was replaced by a laser diode in a laser mount with current and temperature controller (LTC100-B, Thorlabs). Fig. 17 (c) shows the schematic of this beam path. A laser diode with the wavelength of 690 nm (HL6738MG, Thorlabs) was used. The laser light was coupled into a 100 µm core fiber using a focusing lens (f=30 mm). The rest of the optical path stayed almost the same, besides that the focusing lens on the structure was replaced with a lens with a smaller focal length (f=100 mm), to get focus on the structure with a diameter similar to the first setup. The polarizer was put after the focal lens to avoid back reflection effects between collimating and focusing lens. Finally, the wavelength filter before the power sensor could be left out here. The change of the white light source with a coherent laser light source was performed to proof that the usage of a wavelength filter with a bandwidth of 40 nm did not impact the power measurement results by measuring higher power in specular reflection than in the first diffraction order reflection. For the

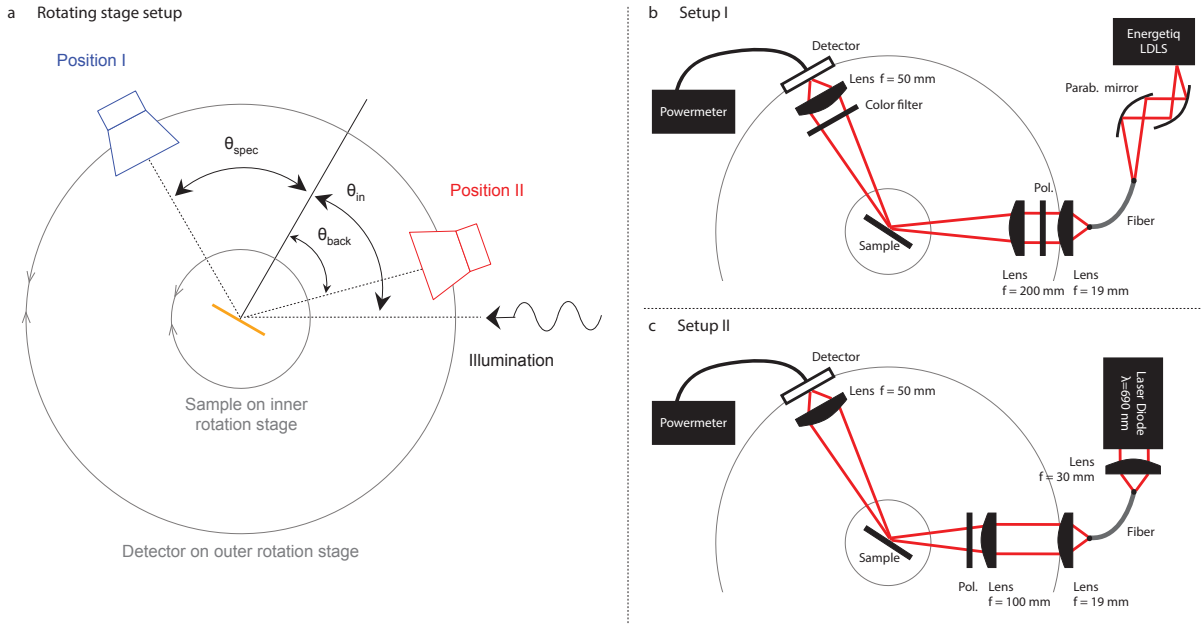

Figure 17: Schematic of the measurement setup and the optical beam paths (a) Angle of illumination θ_{in} can be changed by rotating the sample on the inner rotating stage while the illumination arm is kept fixed. The coupling intensity to the different diffraction orders is measured by independently rotating the detector on the outer rotating stage to positions I to measure θ_{out} or position II to measure θ_{back}. (b) Schematics of optical beam paths of the setup using a broadband light source (Setup I). White light from a LSDL is coupled to the fiber by two parabolic mirrors. An optical filter is mounted in front of the detector, to choose the measured wavelength. (c) Schematics of optical beam paths of the setup using a laser diode (Setup II). Red light (λ=690 nm) is coupled to the fiber by a focusing lens.

intended design we chose a period of Λ=600 nm to enable efficient reflection towards the first diffraction order in the free-space wavelength range λ =490 - 940 nm. Fabricated was a sample with a period of 601-605 nm. This deviation is expected due to the accuracy of electron beam writing processes of ±5 nm. The length of a unit cell was determined in two different ways. First, in a top-view SEM image of the sample the distance between 15 unit cells has been determined by electron micrographs and lead to an length of the unit cell of 605±1 nm. Second, using a least-squares fit the grating equation for the order m=-1 was fitted to the measured incident and diffracted angles θ_{in} and θ_{out} of the optical measurement that is described in chapter 5.3.1. From the diffraction equation (1) follows:

$$\theta_{out} = \arcsin(\sin(\theta_{in}) + \frac{m\lambda}{\Lambda}) \tag{14}$$

The outgoing angle of the first negative diffraction order (m=-1) of the structure was measured with a wavelength of λ=700 nm. In this way the period of the structure was determined to be 600.9±0.5 nm. The SEM image of the first method and the fit to the data points are shown in the appendix in Fig. A2.

5.3 Optical response of graded metasurface

5.3.1 Coupling efficiency at ideal wavelength

The diffraction response of the device at a wavelength of λ=700 nm is quantitatively demonstrated in Fig. 18. Owing to the scattering symmetry of the device imposed by reciprocity, the measurement process could be reduced to only half of the angular range, but to confirm the theoretical results measurements were performed across the entire angular spectrum. In the figure, the specular reflection is compared to the measurements obtained using a flat silver mirror, similar to the ground plane utilized in the device, allowing a direct comparison that provides a quantitative calibration of the measured efficiency. The grey circles in Fig. 18 present the measured angular response of the silver mirror when illuminated with s-polarized light at λ=700 nm. Around 10% of the incident power is absorbed in the silver or lost through diffused scattering. The measured response of the silver mirror is slightly lower than the simulated one, also shown in Fig. 18. This is due to the roughness of the surface by evaporation which leads to the creation of surface plasmon polaritons and therefore to absorption and scattering. The level of reflectivity of the sample to the first diffraction order is shown with red circles in Fig. 18, demonstrating that most of the scattered light is indeed efficiently reflected toward the diffraction order. In addition, with the dielectric metasurface in place, specular reflection significantly drops over a wide angular region around the retroreflective angle of 35.7°. The scattered power is focused toward the backward diffraction channel (s_1^- in Fig. 1), yielding a coupling

efficiency of 88% under illumination at $\theta_{in} = 35.7°$. Consistent with the absorption level obtained from the bare silver back-mirror, less than 10% of the impinging power is absorbed or diffusely scattered at the design frequency under illumination from all angles, except around the Wood's anomaly, the well known grating anomalies caused by surface plasmon polaritons [40].

Here, increasing the incidence angle toward grazing angles has an effect on the overall back reflection efficiency, but, up to a remarkably large angle $\theta_{in} = 75°$, at λ=700 nm the dominant portion of the scattered power remains in the same half-plane of the incident wave. For illumination at angles less than $\theta_{in} < 9°$ degrees, the second scattering channel is non-radiative for λ=700 nm, and thus it is not excited, consistent with the calculated results in Fig. 4. Over this range, the metasurface operates as a simple mirror, as observed in Fig. 18.

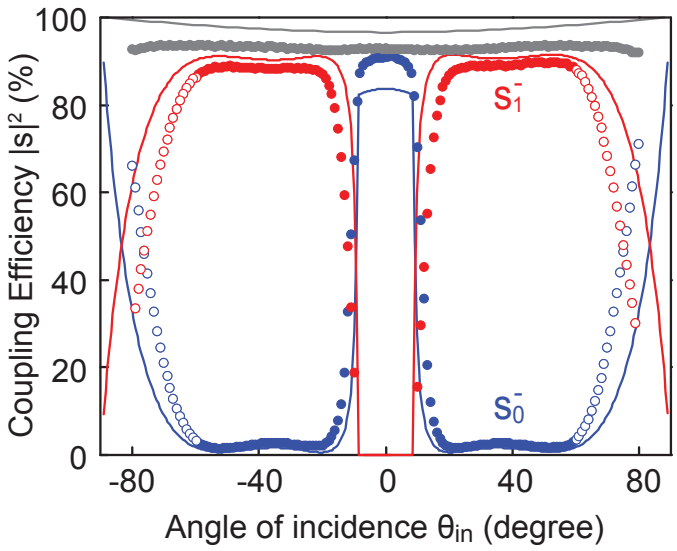

Figure 18: Back-reflection response of the fabricated device Angular response at λ=700 nm. Comparison between measurements (circles) and numerical FEM simulations (solid lines)(Simulations: see chapter 4.1.1). Coupling efficiencies for the specular reflection s_0^+ and the first-order negative reflection s_1^-, are shown with blue and red colors, respectively. The empty circles indicate reflection measurements for angles above $|\theta_{in}| = 60°$, for which the spot size of the beam is larger than the structure and part of the beam is specularly reflected by the mirror next to the structure. The measurements and simulations of the bare mirror are depicted in grey. The flat surface supports specular reflection with approximately 10% absorption across all angles.

For comparison, the solid lines in Fig. 18 show the calculated coupling to the two scattering orders obtained using full-wave simulation for a structure with the same geometry as the fabricated device (See chapter 4.1.1). The simulated results agree very well with

the experiment, even though a slightly lower cut-off at large angles is observed in the measured data compared to the calculated curves. This is due to the small size of the sample, as the area where the measurement beam hits the structure increases with higher incoming angles and exceeds the structure area for $\theta_{in} > 60°$. In this angular range, part of the light is specularly reflected by the bare mirror next to the structure. This effect can be corrected by either reducing the size of the focal point or by increasing the area of the structure. In chapter 5.3.5 a sample with an area of 2 x 2 mm^2 was measured, which results in a high efficient coupling towards the first negative diffraction up to higher angles. Another evident difference between simulation and measurement in Fig. 18 is the higher coupling efficiency of the measurement compared to the calculation in the specular reflection for angles between $\theta_{in} = 9°$ and $\theta_{in} = -9°$. As mentioned earlier (Chapter 4.1.2), the specular reflection for small incoming angles in between the cut-off angles is calculated differently with two simulation methods. The FDTD results of chapter 4.1.2, Fig. 13 (a) corresponds more accurately to the measured values than the specular reflection obtained by FEM. First, it was suspected that the measured power in specular reflection is too high as the used color filter for the measurement with the broadband light source has a width of 40 nm and extra power of this bandwidth is only measured in specular reflection but not in diffraction. However, this could be refuted by repeating the measurement with a monochromatic light source (Setup II, see Fig. 17), where a high intensity in specular reflection for small incoming angles could be observed as well. It is not clear at this point of the work what the origin of the difference in angular response between $\theta_{in} = 9°$ and $\theta_{in} = -9°$ is.

A remarkable property of the proposed device consists in its broadband operation, which is attributed to the non-resonant nature of the involved scattering phenomenon, based on the phase gradient imposed through the metasurface. While the surface impedance of the trapezoids is expected to change over frequency, its relative slope across each unit cell is not significantly affected by frequency variations, ensuring that the net momentum imparted to the impinging wave still funnels most of the energy back to the first diffraction order. To further investigate this property, the amplitude dispersion of the coupling to the two scattering modes for a structure with the dimensions of the fabricated device through full-wave simulations for all incident angles was determined as described in 4.2.3. As expected, the designed metasurface operates over an extremely broad half-power wavelength range λ=490-940 nm in terms of back reflection efficiency. This simulations were verified with experimental measurements at multiple wavelengths, in addition to the λ=700 nm case, as reported in the following chapter.

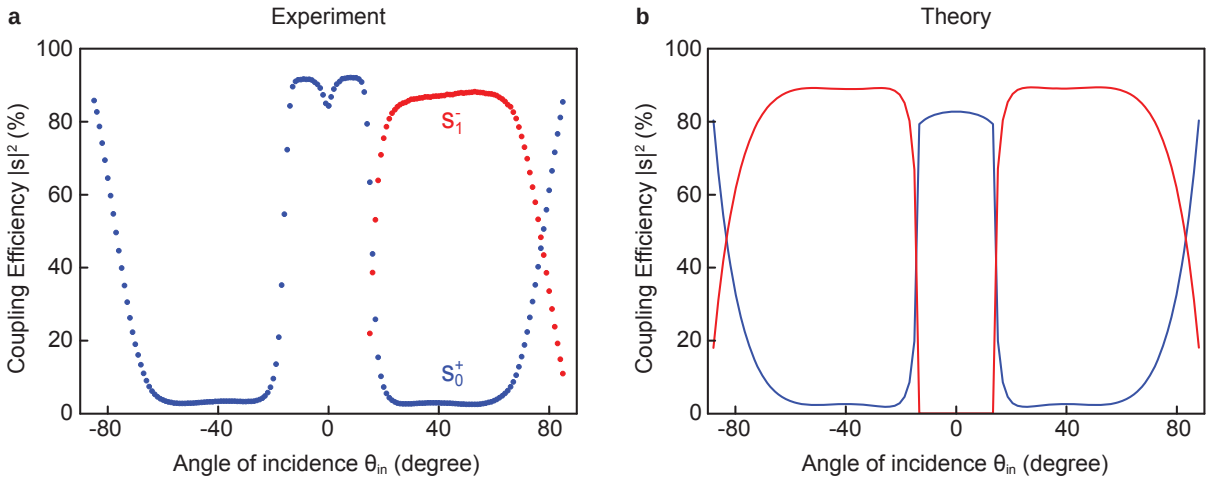

Figure 19: Angular response at 750 nm Coupling efficiencies for the specular reflection s_0^- (blue) and the first-order negative reflection s_1^- (red), are shown: (a) Measurement (circles) and (b) numerical analysis of the structure with the fabricated dimensions (solid lines).

5.3.2 Coupling efficiency at different wavelengths

In addition to the measurements performed at λ=700 nm on the fabricated sample, the broadband operation of the retroreflector is verified through analogous measurements at λ=750 nm and λ=850 nm. The angular response at these wavelengths was obtained using the broadband light source and choosing the color filter of the respective wavelength of interest. The results are compared with full-wave COMSOL simulations (see chapter 4.1.1) of the retroreflective metasurface, with dimensions obtained from the fabricated device and are shown in Fig. 19 (λ=750 nm) and 20 (λ=850 nm). At λ=750 nm the measurement campaign is performed only for half of the angular spectrum. As discussed in chapter 2.3, reciprocity ensures that the distribution of the scattering amplitudes are symmetric with θ_{in}. The small irregularities observed in the measurement close to normal incidence are associated with polarization impurity of the incident light. Due to non-ideal alignment of the polarizer, the incident beam may contain a fraction of p-polarized light.

5.3.3 Polarization dependence of the back reflector

The metasurface was specifically tailored for s-polarized light, i.e., light with electric field vector parallel to its plane. For s-polarized illumination, the majority of the incident wave is redirected toward the first diffraction order (which lies in the same half-plane as the incident one), creating a negative reflection effect. This effect is supported by the tailored distribution of the local reflection coefficient for this polarization. On the other hand, under p-polarization the surface elements experience different local reflection

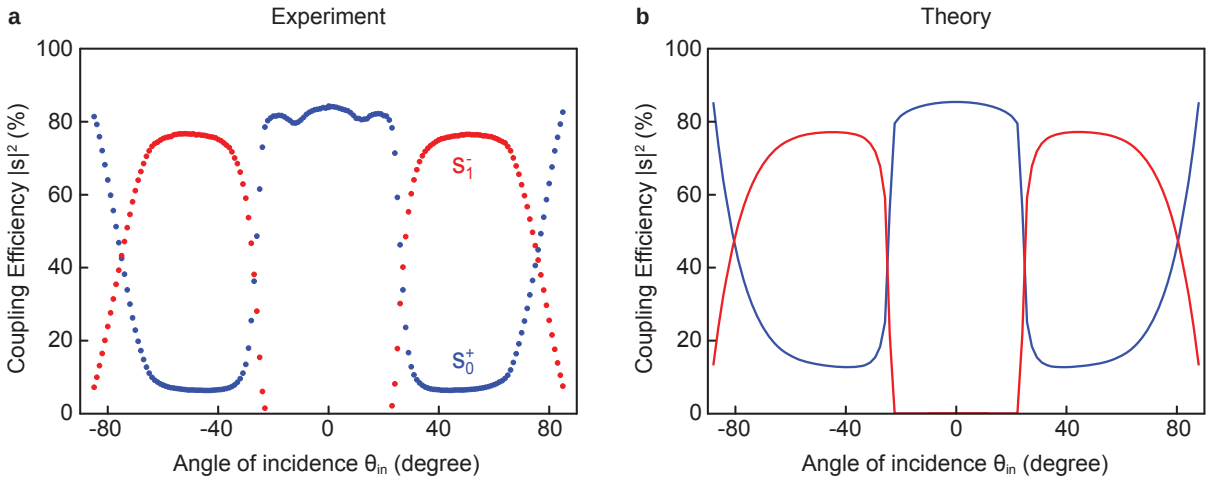

Figure 20: Angular response at 850 nm Coupling efficiencies for the specular reflection s_0^- (blue) and the first-order negative reflection s_1^- (red), are shown: (a) Measurement (circles) and (b) numerical analysis of the structure with the fabricated dimensions (solid lines).

phases due to their anisotropy. For p-polarized illumination, the surface is approximately a mirror, with around 15% coupling toward the non-specular diffraction channel and 15% absorption (Fig. 21 (a)).

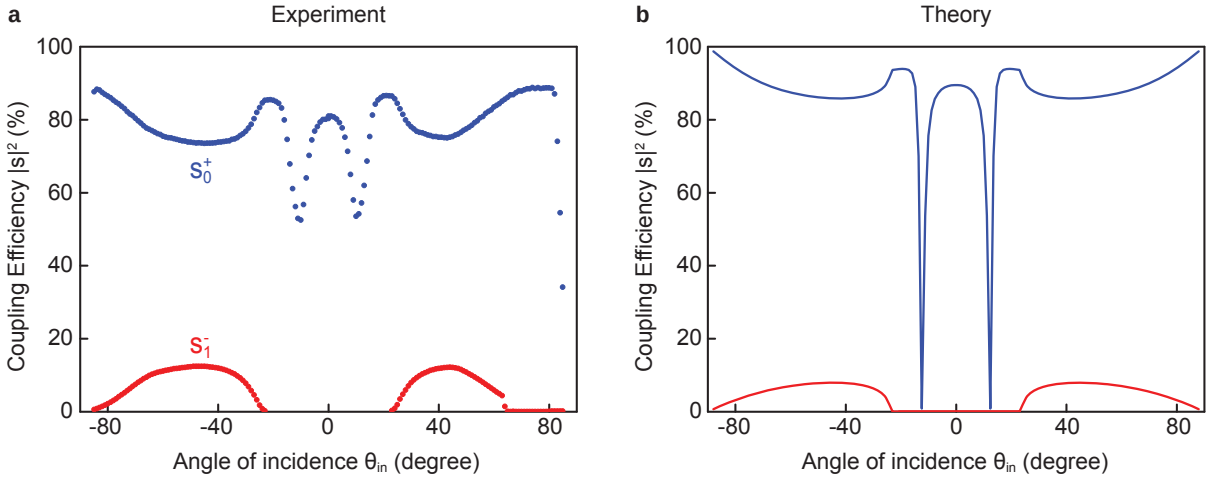

Figure 21: Angular response at 850 nm Scattering response for p-polarized illumination at 850 nm. Side-by-side comparison between (a) measurement (circles) and (b) numerical analysis (solid lines) of the fabricated device under p-polarized illumination. Specular reflection s_0^- and the first-order negative reflection s_1^-, are shown with blue and red colors, respectively.

In addition, the measurements reveal the presence of a critical incident angle for this polarization. At this angle, the incident light experiences enhanced absorption, confirmed by the corresponding simulations shown in Fig. 21 (b). This enhanced absorption peak is attributed to critical coupling between the free space mode and a grating resonance

at the glass-silver interface. We also note that by using isotropic surface elements in proper 2D arrangements, the metasurface can be designed to operate isotropically for both polarizations and 3D illumination angles [8]. Currently this possibility is explored to create polarization insensitive back-reflectors.

5.3.4 Laser diode measurement for result confirmation

To varify the measurements with the broadband light source, the measurement was repeated on the same sample using a laser diode with a wavelength of λ=690 nm. This measurement was performed particularly, to check if the difference of the coupling efficiency in the specular reflection for angles between $\theta_{in} = 9°$ and $\theta_{in} = -9°$ still exceeds the expected efficiency from the simulation. The results of the measurement are depicted in Fig. 22, next to the measurement using the broadband source from chapter 5.3.1 (transparent lines). In the figure it can be seen that both measurements show the same trends. The response of the two measurements show the same coupling efficiency for specular as well as first order reflection. As mentioned above the reflection in specular reflection between $\theta_{in} = 9°$ and $\theta_{in} = -9°$ is again higher than predicted in simulations and is therefore not an effect of the bandwidth of the filter in the measurement setup with the broadband light source. The angular shift that can be observed for the laser measurement compared to the white light source measurement might be due to a slightly different alignment of the rotating stage setup in this measurement.

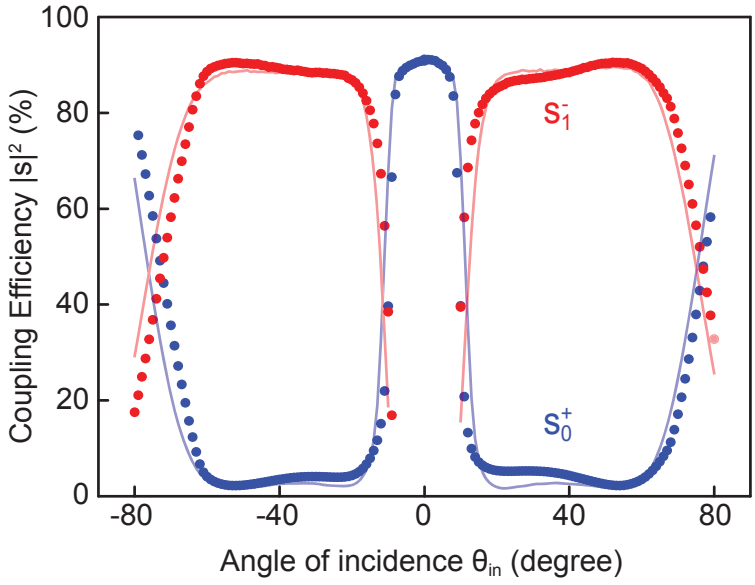

Figure 22: Angular response at 690 nm Measurement with Laser diode at 690 nm (circles) and with broadband source and filter at 700 nm (transparent lines). Specular reflection s_0^- and the first-order negative reflection s_1^-, are shown with blue and red colors, respectively.

5.3.5 Coupling efficiency for N=2 and N=3 discretization

For the sample in the previous measurements the ideal phase profile has been discretized into three steps to achieve N=3 phase regions with different effective index on the substrate. Reducing the discretization to N=2 phase regions leads theoretically to a decrease in efficiency of the back reflection to 75% as calculated in chapter 2.4. Implementing this in a fabricated sample, following the same approach as before, suggests that instead of two TiO_x nanorods only one nanorod is placed per unit cell on the protected silver mirror, to create two discrete regions. To compare the performance of a structure with one and two lines, two samples have been fabricated in parallel, one in the same design as before, and one where only the taller rod, with the same dimensions as in the N=3 design, is placed on the mirror. The structures have a size of 2x2 mm^2 on those samples, which gives the possibility to measure reliable until $\theta_{in} = 68$ degrees. The measurements on both structures have been performed using the broadband light source with a filter for $\lambda = 700\,nm$, and the results of the angular response are depicted in Fig. 23 (a). SEM images of the two different structures are depicted in Fig. 23 (b) for the structure with N=2 discretization steps and therefore one TiO_x line per unit cell and in Fig. 23 (c) for the structure with N=3 discretization steps and two TiO_x lines per unit cell. The structure in (c) has the same design as in the sample of the measurements of the previous chapters. The enhanced area size of this structure is obvious in the measurements as the angle range for efficient coupling (>85%) is increased towards higher angles for the sample with N=3 discretization steps. The effect of the reduction to only one line in the sample has already been studied in simulations before (Chapter 4.2.2) and it was seen that simulations do not show a reduction in efficiency if only one TiO_x rod is placed on the surface, as it would be expected following form the calculations in chapter 2.4. The comparison of the angular response in Fig. 23 matches the results of the simulations. In the measurement, the total reflection of the sample with N=3 steps was reduced as there were fabrication defects on the structure (See Fig. A3 for original data). Therefore, in Fig. 23 the coupling efficiency of the sample with N=3 is normalized to the coupling efficiency of the sample with N=2 at 0 degrees. The coupling efficiency to the first negative diffraction order reaches higher values for the sample with N=2 for $\theta_{in} = 21.5 - 51.5$ degrees, up to 94.5%. The coupling efficiency of the sample with N=3, however, stays at a high level up to high angles around $\theta_{in} = 68$ degrees. As the measurement of the structure with N=3 was normalized, no specific efficiency is stated here.

We can see from the results of this measurements and the simulation of chapter 4.2.2 that it is not possible to directly implement the discretization of the phase profile as calculated in 2.4 to a design for fabrication with a discretization of the effective index. While the measurements in chapter 18-22 match the expectations of the calculation of the coupling

efficiency for a discretized phase profile with N=3 discretization steps in chapter 2.4, the reduction to only N=2 discretization steps seems not fulfilled by excluding the smaller TiO_x line in the fabricated device. The achieved coupling efficiency toward the negative diffraction order of the N=2 design even exceed the coupling efficiency in the N=3 for angles between $\theta_{in} = 21.5 - 51.5$ degrees.

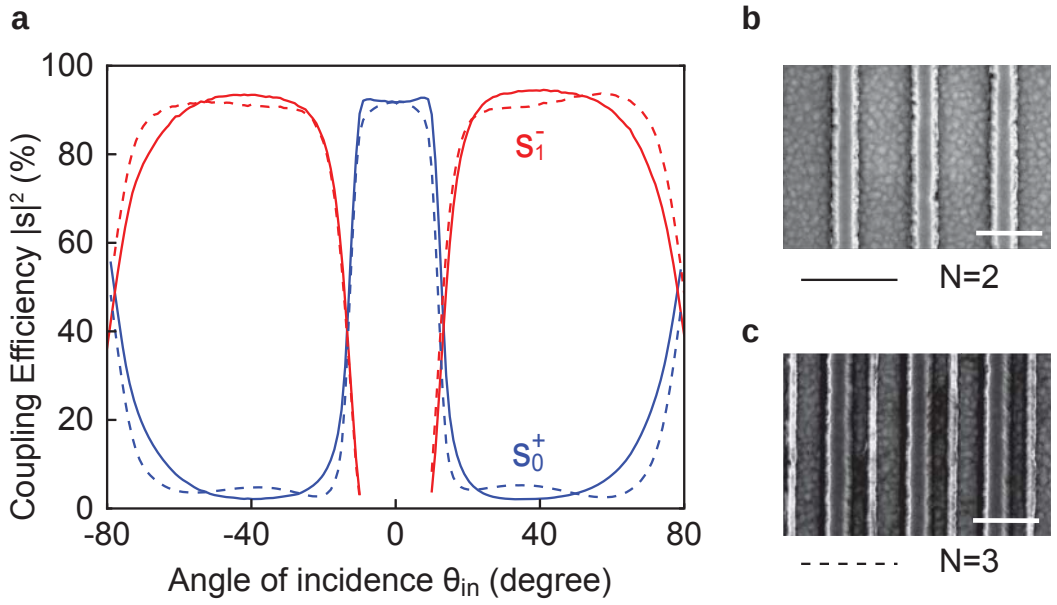

Figure 23: Comparison of structures with N=2 and N=3 (a) Angular response at 700 nm for structure with N=2 (solid lines) and of structure with N=3 (dashed lines). Coupling efficiency toward the specular reflection s_0^- (blue) and the first-order negative reflection s_1^- (red) are shown. The measurement of the structure with N=3 is normalized to the coupling efficiency of the sample with N=2 at 0 degrees. (b) SEM top-view of sample with N=2 and one TiO_x line per unit cell. (c) SEM top-view of sample with N=3 and two TiO_x lines per unit cell. Scale bar is 500 nm.

6 Discussion, conclusion and outlook

In this work the concept of a gradient metasurface has been used to engineer a wide-angle, broadband back-reflector. First, the theoretical phase profile of the surface was analytically derived, using a ray-optics approach and full wave derivations were performed. Next, a realizable design was developed by transforming the gradient phase profile into a discretized surface with an effective index gradient. The metasurface, comprised of an assymmetric high-index TiO_x grating on a protected mirror, was fabricated by using nanofabrication tools. Afterwards, the coupling efficiency towards the first diffraction order was measured in an optical rotating stage setup and simulated using COMSOL and FDTD Lumerical. Several properties like angular response, behavior at different wavelengths, polarization dependence and discretization sensitivity were investigated during this work. The results obtained from optical experiments and simulations confirm the theoretical calculations and proof that the usage of the Huygens-Fresnel principle presents a powerful tool to design reflective surfaces at will.

The properties of the structure are very desirable from a practical standpoint, indicating that there is no trade-off between directionality and efficiency in the proposed metasurface, and back reflection to the first negative order can be achieved over a broad range of angles, even significantly away from the normal. This property also suggests an interesting possibility for applications as retroreflectors. For detectors using narrowband illumination and a relatively wide collection aperture this surface can reflect nearly all of the impinging energy back to the source. Another interesting application of this surface might be replacing diffusive retroreflective tapes (over a limited angle), as the efficiency of reflection is significantly larger than available reflective tapes and the metasurface can be tailored to operate for extremely broad AOI range [28]. The angular robustness of the metasurface response, associated with its non-resonant performance properties, is reflected in an inherently broadband operation [8], and is robust against minor variations in the spatial phase profile.

In the context of retroreflection, it should also be noticed that a grating-based retroreflector (for AOI close to retroreflective angle) does not impose the typical lateral shift present in 3D retroreflectors. The response of the designed metasurface is also controllable with the polarization of the incident wave. The surface features utilized for this implementation are anisotropic, as their scattering properties depend on the orientation of the field vectors, and the local reflection phase is approximately constant for p-polarized illumination. Consequently, the surface operates as a simple mirror for this polarization. In other words, this metasurface selectively reflects in opposite half-planes the two impinging polarizations. Polarization independent designs of back-reflecting metasurfaces are cur-

rently investigated, based on a similar principle, achieved by considering 2D arrangements of isotropic surface elements [8, 12].

We have highlighted significant advantages in terms of size, simplicity of fabrication, integrability, bandwidth, acceptance angular range, low-profile and efficiency of the proposed back-reflective metasurface, designed and realized based on the gradient metasurface concept. We believe that this approach may become an effective replacement of conventional bulky optical elements, particularly for subwavelength gratings, extensively used in pulse shaping and spectrum splitting applications. The design is based on the Huygens-Fresnel principle and is scalable over different frequency ranges. Similar designs may be explored at radio-frequencies to improve passive and active RFID tags. The control of the angle of reflection may also enable applications for light management in solar cells. The thin metasurface profile allows spin coating of an absorber material on top of the metasurface, which may enable broadband enhanced light trapping and absorption [8]. More broadly, our study demonstrates an exciting application of nanostructured gradient metasurfaces, which does not present the common trade-off between efficiency, bandwidth and robustness, with direct implications in a variety of nanophotonic applications.

A Appendix

A.1 Determination of dielectric constants of TiO_x using ellipsometry

Ellipsometry is a well known technique for determining the refractive index of a material [41]. In this case, a 130 nm thick TiO_x layer was evaporated on a Si wafer in the same evaporation step as in the fabrication of the samples for the optical measurement. Reflection from the sample around the Brewster angle (at 69 degrees, 74 degrees and 79 degrees) were measured for wavelengths between λ=300 nm and λ=1000 nm in steps of 5 nm. A combined Cauchy and Gaussian oscillator fit was used to determine the refractive index n and extinction coefficient k of TiO_x. With values between n=2.35 for λ=500 nm and n=2.23 for λ=1000 nm, n is close to constant for $\lambda > 500$ nm and k is close to zero for wavelengths above 400 nm. In Fig. A1 n and k are plotted.

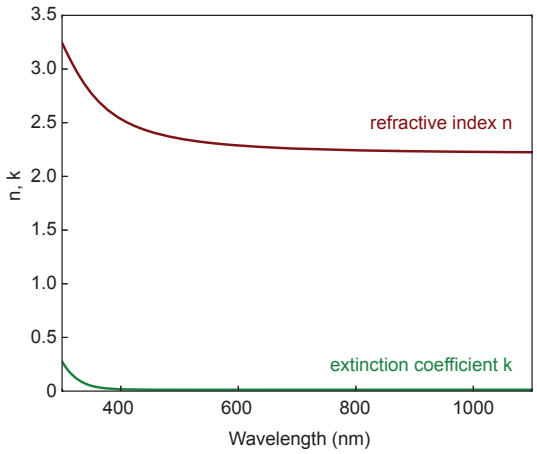

Figure A1: Refractive index and extinction coefficient of TiO_x. Refractive index n (red) and the extinction coefficient k (green) of TiO_x were determined by spectroscopic ellipsometry.

A.2 Determination of period of fabricated structure

The period of the structure was initially designed to be 600 nm. However, the accuracy of electron-beam lithography is restricted, depending on the alignment of the electron-beam. The final period was determined in two ways, by measuring the distance of several periods in an SEM image (Fig. A2 (a)) and by fitting the diffraction equation to the reflected and incident angles (Fig. A2 (b)) as described in the main text.

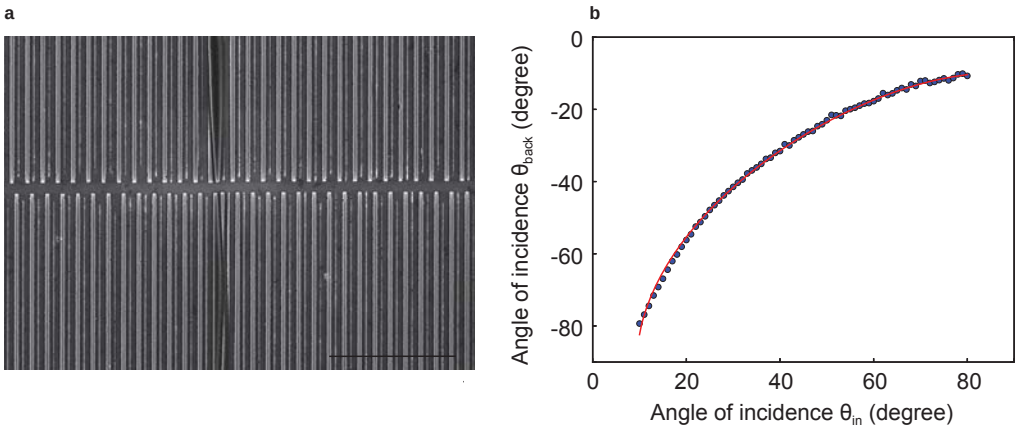

Figure A2: Determination of period Λ of fabricated sample (a) Top view SEM image of fabricated structure for determination of period by electron micrographs. Scalebar is 5 µm. (b) Least square fit of grating equation to incident angles θ_{in} and back reflected angles θ_{back} toward the first negative diffraction order.

A.3 Original data of optical measurement of structure with N=2 and N=3

The angular response for the structure with N=2 and N=3 discretization, discussed in chapter 5.3.5, was normalized on the coupling efficiency of specular reflection at $theta_{in}$=0 degrees. In Fig. A3, the data with the original measured efficiency is shown. The high difference in coupling efficiency results from a defect in the N=3 structure, where the surface of the sample is damaged.

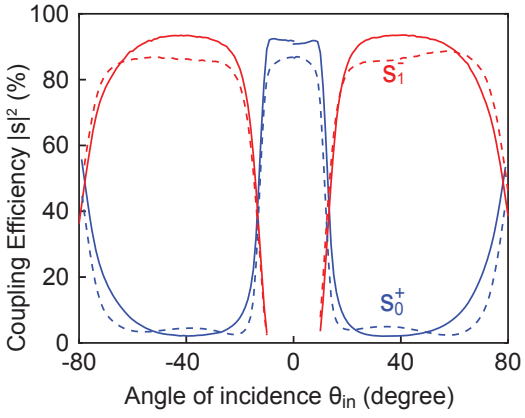

Figure A3: Original data of comparison of structures with N=2 and N=3 Angular response at 700 nm for the structure with N=2 (solid lines) and of the structure with N=3 (dashed lines). Coupling efficiency toward the specular reflection s_0^- (blue) and the first-order negative reflection s_1^- (red) are shown.

This thesis is based on the following publication (in preparation):

Wide-Angle, Broadband Graded Metasurface for Back Reflection, N. M. Estakhri, V. Neder, M. W. Knight, A. Polman, and A. Alù, in preparation.

This thesis is the result of a cooperation between the Metamaterials & Plasmonics Research Laboratory at the University of Texas at Austin and the Photonic Materials Research Group at FOM Institute AMOLF in Amsterdam. The theoratical work and the FEM simulations are developed by Nasim Mohammadi Estakhri and Andrea Alù from the University of Texas. The fabrication, the FDTD simulations and the optical measurements have been done by Verena Neder under supervision of Mark W. Knight and Albert Polman at FOM Insitute AMOLF.

References

[1] N. I. Zheludev and Y. S. Kivshar, "From metamaterials to metadevices," *Nature Materials*, vol. 11, pp. 917–924, oct 2012.

[2] D. Lin, P. Fan, E. Hasman, and M. L. Brongersma, "Dielectric gradient metasurface optical elements," *Science*, vol. 345, pp. 298–302, jul 2014.

[3] N. Yu and F. Capasso, "Flat optics with designer metasurfaces," *Nature Materials*, vol. 13, pp. 139–150, jan 2014.

[4] M. Khorasaninejad, W. T. Chen, R. C. Devlin, J. Oh, A. Y. Zhu, and F. Capasso, "Metalenses at visible wavelengths: Diffraction-limited focusing and subwavelength resolution imaging," *Science*, vol. 352, pp. 1190–1194, jun 2016.

[5] N. Yu, P. Genevet, M. A. Kats, F. Aieta, J.-P. Tetienne, F. Capasso, and Z. Gaburro, "Light Propagation with Phase Discontinuities: Generalized Laws of Reflection and Refraction," *Science*, vol. 334, pp. 333–337, oct 2011.

[6] X. Ni, A. V. Kildishev, and V. M. Shalaev, "Metasurface holograms for visible light," *Nature Communications*, vol. 4, pp. 1–6, nov 2013.

[7] G. Zheng, H. Mühlenbernd, M. Kenney, G. Li, T. Zentgraf, and S. Zhang, "Metasurface holograms reaching 80% efficiency," *Nature Nanotechnology*, vol. 10, pp. 308–312, feb 2015.

[8] N. M. Estakhri and A. Alu, "Ultra-Thin Unidirectional Carpet Cloak and Wavefront Reconstruction With Graded Metasurfaces," *IEEE Antennas and Wireless Propagation Letters*, vol. 13, pp. 1775–1778, 2014.

[9] X. Ni, Z. J. Wong, M. Mrejen, Y. Wang, and X. Zhang, "An ultrathin invisibility skin cloak for visible light," *Science*, vol. 349, pp. 1310–1314, sep 2015.

[10] B. Orazbayev, N. Mohammadi Estakhri, M. Beruete, and A. Alù, "Terahertz carpet cloak based on a ring resonator metasurface," *Physical Review B*, vol. 91, p. 195444, may 2015.

[11] C. Pfeiffer and A. Grbic, "Metamaterial Huygens' Surfaces: Tailoring Wave Fronts with Reflectionless Sheets," *Physical Review Letters*, vol. 110, p. 197401, may 2013.

[12] A. Pors and S. I. Bozhevolnyi, "Plasmonic metasurfaces for efficient phase control in reflection," *Optics Express*, vol. 21, p. 27438, nov 2013.

[13] Y. Hadad, D. L. Sounas, and A. Alu, "Space-time gradient metasurfaces," *Physical Review B*, vol. 92, p. 100304, sep 2015.

[14] Y. Shi and S. Fan, "Dynamic non-reciprocal meta-surfaces with arbitrary phase reconfigurability based on photonic transition in meta-atoms," *Applied Physics Letters*, vol. 108, p. 021110, jan 2016.

[15] Z. Wei, H. Li, C. Wu, Y. Cao, J. Ren, Z. Hang, H. Chen, D. Zhang, and C. T. Chan, "Anomalous reflection from hybrid metamaterial slab," *Optics Express*, vol. 18, p. 12119, jun 2010.

[16] X. Su, Z. Wei, C. Wu, Y. Long, and H. Li, "Negative reflection from metal/graphene plasmonic gratings," *Optics Letters*, vol. 41, p. 348, jan 2016.

[17] Z.-l. Deng, S. Zhang, and G. P. Wang, "A facile grating approach towards broadband, wide-angle and high-efficiency holographic metasurfaces," *Nanoscale*, vol. 8, no. 3, pp. 1588–1594, 2016.

[18] J. Du, Z. Lin, S. T. Chui, W. Lu, H. Li, A. Wu, Z. Sheng, J. Zi, X. Wang, S. Zou, and F. Gan, "Optical Beam Steering Based on the Symmetry of Resonant Modes of Nanoparticles," *Physical Review Letters*, vol. 106, p. 203903, may 2011.

[19] C. Wu, N. Arju, G. Kelp, J. A. Fan, J. Dominguez, E. Gonzales, E. Tutuc, I. Brener, and G. Shvets, "Spectrally selective chiral silicon metasurfaces based on infrared Fano resonances," *Nature Communications*, vol. 5, pp. 1–9, may 2014.

[20] M. Rumpel, M. Moeller, C. Moormann, T. Graf, and M. A. Ahmed, "Broadband pulse compression gratings with measured 997% diffraction efficiency," *Optics Letters*, vol. 39, p. 323, jan 2014.

[21] N. Destouches, A. V. Tishchenko, J. C. Pommier, S. Reynaud, O. Parriaux, S. Tonchev, and M. A. Ahmed, "99% efficiency measured in the -1st order of a resonant grating," *Optics Express*, vol. 13, no. 9, p. 3230, 2005.

[22] M. Flury, A. V. Tishchenko, and O. Parriaux, "The Leaky Mode Resonance Condition Ensures 100% Diffraction Efficiency of Mirror-Based Resonant Gratings," *Journal of Lightwave Technology*, vol. 25, pp. 1870–1878, jul 2007.

[23] S. Astilean, P. Lalanne, P. Chavel, E. Cambril, and H. Launois, "High-efficiency subwavelength diffractive element patterned in a high-refractive-index material for 633 nm," *Optics Letters*, vol. 23, p. 552, apr 1998.

[24] E. Loewen and E. Popov, *Diffraction Gratings and Applications*. Marcel Dekker, Inc., 1997.

[25] C. Holloway, M. Mohamed, E. Kuester, and A. Dienstfrey, "Reflection and Transmission Properties of a Metafilm: With an Application to a Controllable Surface Composed of Resonant Particles," *IEEE Transactions on Electromagnetic Compatibility*, vol. 47, pp. 853–865, nov 2005.

[26] N. M. Estakhri and A. Alù, "Recent progress in gradient metasurfaces," *Journal of the Optical Society of America B*, vol. 33, p. A21, feb 2016.

[27] V. H. Rumsey, "Reaction Concept in Electromagnetic Theory," *Physics Review*, vol. 94, no. 1483, p. 1705, 1954.

[28] G. Whitman and F. Schwering, "Reciprocity identity for periodic surface scattering," *IEEE Transactions on Antennas and Propagation*, vol. 27, pp. 252–254, mar 1979.

[29] H. Zappe, *Fundamentals of Micro-Optics*. Cambridge University Press, 2010.

[30] I. Hotovy, I. Kostic, P. Nemec, M. Predanocy, and V. Rehacek, "Patterning of titanium oxide nanostructures by electron-beam lithography combined with plasma etching," *Journal of Micromechanics and Microengineering*, vol. 25, p. 074006, jul 2015.

[31] I. Hotovy, S. Hascik, M. Gregor, V. Rehacek, M. Predanocy, and A. Plecenik, "Dry etching characteristics of TiO2 thin films using inductively coupled plasma for gas sensing," *Vacuum*, vol. 107, pp. 20–22, sep 2014.

[32] M. Shearn, X. Sun, M. D. Henry, A. Yariv, and A. Scherer, "Advanced Plasma Processing: Etching, Deposition, and Wafer Bonding Techniques for Semiconductor Applications," in *Semiconductor Technologies*, InTech, 2010.

[33] M. A. van de Haar and A. Polman, "Fabrication process of a coaxial plasmonic metamaterial," *Optical Materials Express*, vol. 6, p. 884, mar 2016.

[34] J. Parsons, C. Burrows, J. Sambles, and W. Barnes, "A comparison of techniques used to simulate the scattering of electromagnetic radiation by metallic nanostructures," *Journal of Modern Optics*, vol. 57, pp. 356–365, mar 2010.

[35] D. Morris, "Which Electromagnetic Simulator Should I Use?," tech. rep., Keysight Technologies, Lakeside, Cheadle Royal Business Park, Stockport SK8 3GR, 2011.

[36] I. H. Malitson, "Interspecimen Comparison of the Refractive Index of Fused Silica," *Journal of the Optical Society of America*, vol. 55, p. 1205, oct 1965.

[37] A. D. Rakić, A. B. Djurišić, J. M. Elazar, and M. L. Majewski, "Optical properties of metallic films for vertical-cavity optoelectronic devices," *Applied Optics*, vol. 37, p. 5271, aug 1998.

[38] B. Liang, M. Bai, H. Ma, N. Ou, and J. Miao, "Wideband Analysis of Periodic Structures at Oblique Incidence by Material Independent FDTD Algorithm," *IEEE Transactions on Antennas and Propagation*, vol. 62, pp. 354–360, jan 2014.

[39] E. Palik, *Handbook of Optical Constants of Solids*. New York: Academic, 1985.

[40] D. Maystre, *Plasmonics*, vol. 167 of *Springer Series in Optical Sciences*. Berlin, Heidelberg: Springer Berlin Heidelberg, 2012.

[41] H. G. Tompkins and E. A. Irene, *Handbook of Ellipsometry*. New York: William Andrew Publishing, 2005.